Physics of Fluids

RESEARCH ARTICLE | JUNE 16 2023

Flow field characteristics of a 127-pin rod bundle with hexagonal spacer grids ✓

Craig Menezes ✉ ; Trevor Melsheimer ; Yassin A. Hassan

Physics of Fluids 35, 067119 (2023)
https://doi.org/10.1063/5.0154590

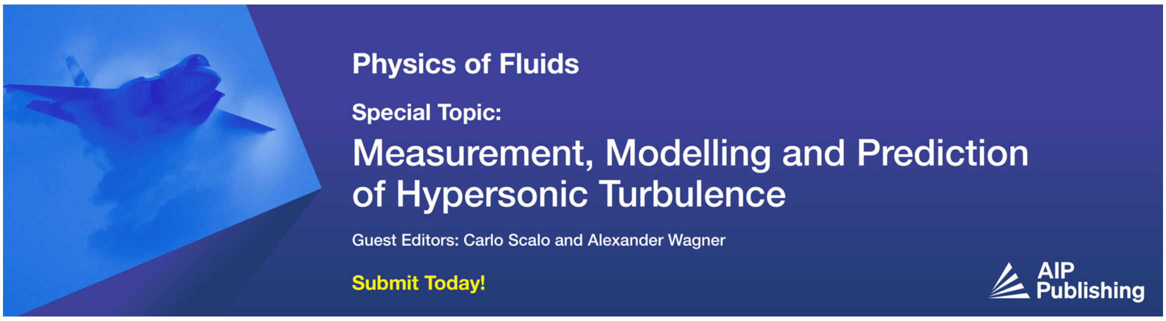

Physics of Fluids ARTICLE pubs.aip.org/aip/pof

Flow field characteristics of a 127-pin rod bundle with hexagonal spacer grids

Cite as: Phys. Fluids **35**, 067119 (2023); doi: 10.1063/5.0154590
Submitted: 14 April 2023 · Accepted: 31 May 2023 ·
Published Online: 16 June 2023

Craig Menezes,[1,a] Trevor Melsheimer,[1,b] and Yassin A. Hassan[2,c]

AFFILIATIONS

[1]Department of Nuclear Engineering, Texas A&M University, 3133 TAMU, College Station, Texas 77843, USA
[2]Department of Nuclear Engineering, J. Mike Walker '66 Department of Mechanical Engineering, Texas A&M University, 3133 TAMU, College Station, Texas 77843, USA

[a]Author to whom correspondence should be addressed: craigmenezes@tamu.edu
[b]Email: trevoram@tamu.edu
[c]Email: y-hassan@tamu.edu

ABSTRACT

A determination of nominal flow phenomena in liquid metal fast reactor (LMFR) fuel assemblies is critical toward generation-IV reactor development. Axially positioned spacer grids are used to maintain the geometry of hexagonal rod bundles and simultaneously introduce perturbations in the flow. Three-dimensional (3D) printed asymmetric honeycomb spacer grids were installed in a prototypical 127-pin LMFR fuel assembly model to study complex fluid dynamics interactions induced by the spacer grid and rods. To characterize flow dynamics in this intricate geometry, time-resolved particle image velocimetry (TR-PIV) using the matched-index-of-refraction method was employed to obtain non-intrusive velocity measurements for three axial planes (one near-wall and two interior planes) at a Reynolds number of 6000. The statistical TR-PIV results compared sub-channel-dependent normalized time-averaged velocity, velocity fluctuations, Reynolds stress, vorticity, and turbulence kinetic energy distributions. TR-PIV line profiles characterized downstream spacer grid flow dynamics. Two-point spatial and spatial–temporal cross-correlation fields revealed local coherent structures and quantified convection velocities of traveling vortices. Spatial–temporal decomposition using dynamic mode decomposition (DMD) applied to the near-wall vorticity fields extracted turbulent structures and flow instabilities in the wake region of the spacer grid, along with their decay and frequency rates. Reduced-order velocity fields from DMD reconstructions identified the most energy-containing coherent structures persistent in the near-wall region. This research provides experimental data sets and analyses of flow behavior in rod bundles with hexagonal spacer grids. The results are critical toward LMFR design and geometry optimization, crucial for the validation of computational fluid dynamics and reduced-order flow models.

NOMENCLATURE

A_{bundle}	Cross-sectional area of the bundle
b	Dynamic mode coefficients
d_p	Seeding particle mean diameter
D	Fuel rod diameter
D_e	Eddy diameter
D_h	Bundle hydraulic diameter
f	Frequency
k	Truncated number of DMD modes
L_c	Characteristic length
N	Total number of TR-PIV snapshots
Q	Flow rate
Re	Reynolds number
R_{uu}	Spatial–temporal) cross-correlation of u'_{rms}
R_{vv}	Spatial–temporal) cross-correlation of v'_{rms}
Stk	Stokes number
u	Instantaneous spanwise velocity
U_0	Bundle-averaged fluid velocity
U_{avg}	Average spanwise velocity
U_c	Convection velocity
U_{mag}	Velocity magnitude
u'_{rms}	Fluctuating spanwise velocity
v	Instantaneous streamwise velocity
V_{avg}	Average streamwise velocity
v'_{rms}	Fluctuating streamwise velocities
X	Spanwise direction
Y	Streamwise direction

α	Image magnification factor
Δt	Interframe time delay
$\tilde{\epsilon}_{N_k}$	Normalized convergence factor
ε	Normalized standard uncertainty
η	Spatial cross-correlation separation distance
λ	DMD Eigenvalues
Θ	Eigenvectors/Exact DMD modes
μ	Dynamic viscosity
μ_r	Index of refraction
χ	Reconstructed TR-PIV velocity from DMD
ρ	Fluid density
ρ_p	Seeding particle density
σ	Standard deviation
τ	Temporal cross correlation time delay
τ_f	Characteristic flow timescale
τ_p	Seeding particle mean response time
Λ	DMD Eigenvalues in phase space
Ω	DMD Eigenvalues in temporal space
ω	Vorticity
$\omega^{\dagger}$	Moore–Penrose pseudoinverse of ω

Acronyms

CFD	Computational fluid dynamics
DMD	Dynamic mode decomposition
LMFR	Liquid metal fast reactor
MIR	Matched-index-of-refraction
PCTD	Pacio-Chen-Todreas Detailed correlation
PIV	Particle image velocimetry
PMMA	Polymethylmethacrylate
POD	Proper orthogonal decomposition
PSD	Power spectrum density
RANS	Reynolds-averaged Navier–Stokes
RMS	Root-mean-square
RPC	Robust phase correlation
SVD	Singular value decomposition
TKE	Turbulence kinetic energy
TR	Time-resolved
UCTD	Upgraded Cheng and Todreas Detailed correlation
VP	Vertical plane
2D2C	Two-dimension two-component
3D	Three-dimensional

I. INTRODUCTION

Understanding fluid dynamics behavior in rod bundle arrangements used by the next generation of nuclear reactors is critical toward the design, optimization, and deployment of novel reactor systems. Liquid metal fast reactors (LMFRs) are one such subcategory of the Generation-IV nuclear reactor designs, employing liquid metals such as lead, sodium, or eutectic alloy mixtures to convert heat from controlled nuclear fission to electricity. The novelty and benefits of LMFR designs include their high-temperature operation, lower operating pressures, and the utilization of the fast neutron spectrum.[1] The cumulative result is a novel reactor design with an improved operational efficiency.

LMFR nuclear fuel rods are typically arranged in a triangular lattice enclosed tightly within a hexagonal duct. The increased packing fraction capitalizes on its fast neutron spectrum operation to obtain a higher power density than traditional reactors.[2] To maintain such a geometrical arrangement and lattice structure, several approaches persist in LMFR core bundle design. The use of thin helically wrapped wires about a rod is one such conception, which also functions as an approach to enhance turbulent mixing.[3] Another method to maintain the geometry of the rod bundle is employing discrete spacer grids installed at several axial locations in the rod bundle. Such spacer grids further function as periodic disturbances in the flow.[4] Spacer grids are further subclassified into honeycomb shaped spacer grids and staggered spacer grids in square or triangular arrays, and may also consist of mixing vanes to enhance the turbulence for improved mixing characteristics.[5–7] Intricacies in the spacer grid design, such as the inclusion of dimples, springs, and support structures, are added features, which enhance their structural stability and address flow induced vibrations.[8] It is imperative to comprehend the fluid dynamics behavior response past installed spacer grids to optimize designs and validate computational models.

The characterization of fluid dynamics and thermal hydraulic effects in hexagonal rod bundle arrangements for LMFR applications has motivated several numerical and experimental investigations. A majority of such research efforts have concentrated on wire-spaced rod bundles—including visualization and thermal-hydraulic investigations by Nguyen *et al.*,[9–11] Childs *et al.*,[12,13] Menezes *et al.*,[14,15] Pacio *et al.*,[16,17] and Song *et al.*,[18–20] among others.[21–23] For discrete hexagonal grid spacers, researchers have investigated spacer grid design influences in a rod bundle from a computational fluid dynamics (CFD) standpoint. Batta and Class[24] performed Reynolds-averaged Navier–Stokes (RANS) CFD simulations on a 19-pin LMFR fuel assembly with grid spacers, for regular and reversed flows through their rod bundle. Mathur *et al.*[25] investigated flow effects for nominal flow and accident conditions due to partial blockages in 19-pin and 127-pin rod bundles with a hexagonal spacer—using a wall-resolved reduced-resolution RANS CFD approach. Their study characterized spanwise and streamwise temperature and velocity variations. To investigate the interlinked thermochemical effects to the velocity distributions, Sergeenko *et al.*[26] performed CFD simulations to characterize physiochemical processes (including oxygen concentrations and oxide film thickness estimations) for a 19-pin LMFR rod bundle using lead-bismuth as the coolant. Scarce experimental research is available in recent literature related to flow dynamics and thermal hydraulics in LMFR assemblies with spacer grids. Experimental tests were performed by Pacio *et al.*[27] to investigate thermal-hydraulic effects in a 19-pin fuel assembly with discrete spacers, using lead-bismuth eutectic alloy as their coolant. Their tests encompassed friction factor estimations using bundle-average pressure drops and heat transfer based on temperature gradients in the rod bundle. These experimental results were also used to validate their computational model predictions for temperature and velocity distributions.[28] Marinari *et al.*[29] studied the thermal hydraulic effects in a 19-pin heated LMFR assembly using both lead and lead-bismuth eutectic alloy as the coolant—to evaluate temperature effects for operating conditions and accident conditions for partially blocked rod bundle configurations. Martelli *et al.*[30] studied natural and forced circulation heat transfer characteristics using lead-bismuth eutectic alloy for a 37-pin hexagonal bundle—arranged in a triangular array using tube grid spacers. In addition to LMFR-specific experimental research, comprehensive tests were performed by

Rehme[4] and Rehme and Trippe[31] to generate extensive databases for pressure drop, friction factor, and velocity profiles. Their tests characterized several spacer grid designs, including honeycomb, triangular, and rhombus spacer grids. Additionally, experimental visualization toward spacer grid research has also been performed for 84-pin gas-cooled fast reactor assemblies with discrete staggered spacers by both Menezes *et al.*[32] and Matozinhos *et al.*[33] It is hence imperative to mitigate the significant gaps in the literature to experimentally characterize flow on encountering hexagonal spacer grids to understand true fluid behavior, spacer grid effects, and the complex fluid interactions within subchannels of a rod assembly.

To understand the local flow phenomena past a honeycomb spacer grid, the presented experimental investigation provides a comprehensive characterization of spacer grid wake effects in a hexagonal rod bundle arrangement. High-fidelity time-resolved particle image velocimetry (TR-PIV) measurements were performed in a prototypical 127-pin liquid metal reactor fuel bundle—presently, the largest PIV experimental LMFR prototypical rod bundle in current existence. 3D printed spacer grids were installed at three distinct locations along the hexagonal rod bundle. PIV experiments were performed for a Reynolds number of 6000 at three distinct axial planes—one plane encompassing the near-wall subchannels and two additional planes passing across the interior subchannels moving closer to the center of the hexagonal rod assembly. To enable the noninvasive flow field measurements in the subchannels of interest, the matched-index-of-refraction (MIR) method was utilized, which allowed an unobstructed view of the subchannels in the 127-pin assembly, with high spatial and temporal resolutions. The experimental facility is described in Sec. II, followed by the TR-PIV methodology in Sec. III. The statistical TR-PIV results are presented in Sec. IV—which detail a comprehensive uncertainty and convergence analysis in Sec. IV A. The first- and second-order flow statistics' contour maps are presented in Sec. IV B along with the TR-PIV line parameter profiles at several axial elevations downstream of the spacer grid. Two-point spatial cross-correlation analysis and spatial–temporal cross-correlation analyses are highlighted in Sec. IV C to capture the spatial extent of turbulent structures and the temporal correlation of the instantaneous spanwise and streamwise velocity components. Section V provides a description and the results obtained from dynamic mode decomposition (DMD) for the near-wall plane vorticity fields to identify the most energy-containing coherent flow structures with a quantification of their stability, decay rates, and temporal characteristics. Section V C 3 also covers DMD flow reconstruction for the near-wall spanwise and streamwise velocity components, yielding reduced-order flow reconstructions of these velocity fields. This experimental investigation provides high-fidelity data sets for fluid dynamics behavior past honeycomb spacer grids in rod bundles and characterizes flow based on the location of the subchannels within such hexagonal assemblies. The results and analyses of this experimental campaign are imperative for the validation and development of CFD and reduced-order models, as well as toward the design and developmental optimization of spacer grids used for LMFR and rod bundle applications.

II. FACILITY DESCRIPTION

A. Test facility

The experimental facility used for the TR-PIV measurements is described in this section. Figure 1 shows the facility with the main components annotated. The facility consists of a test section containing the 127-pin assembly with a primary flow loop to transport the working fluid through the test section. A primary 14.91 kW centrifugal pump operated by a variable frequency drive controls the flow rate of the working fluid through the test section. A Sierra InnovaMass 240i in-line high-precision vortex shedding flow meter, with a full-scale range of 2.05×10^{-3} m^3/s and an accuracy of ±0.7% of the reading, was used to acquire the test volumetric flow rate. A secondary flow loop controls the temperature of the working fluid in the test facility. The surge tank with a 0.4 m^3 volumetric capacity functions as storage for the working fluid and to dampen flow oscillations and fluctuations during the experiments.

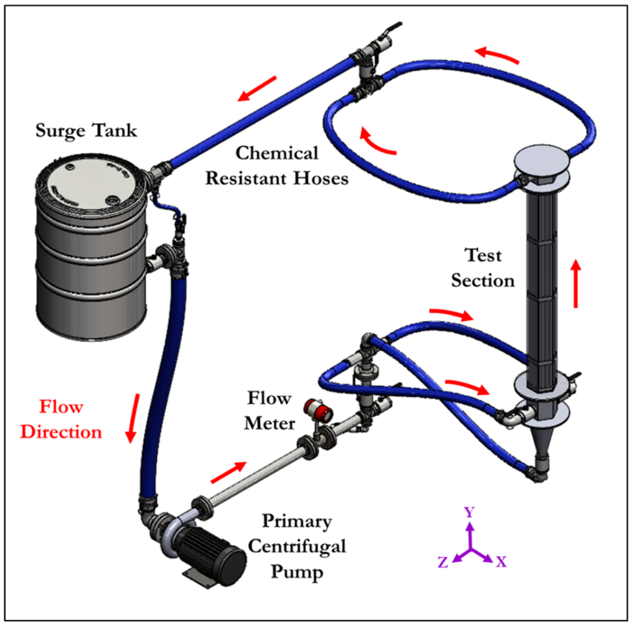

FIG. 1. 127-pin prototypical rod bundle experimental test facility overview.

The test section was designed to ensure mechanical and vibrational isolation, simultaneously using chemically resistant components to prevent chemical interactions with the working fluid and the facility components. Fluid enters the test section initially through a honeycomb grid flow straightener installed near the lower test section plenum to assist in flow straightening.

The matched-index-of-refraction (MIR) method was utilized in the presented experimental tests to obtain clear, unobstructed PIV images in the flow visualization region. The MIR approach relies on the matching of the optical indices of refraction of the solid structural components of the test section and the working fluid. This allows velocimetry measurements in complex, intricate and difficult-to-access geometries, such as subchannels in the 127-pin assembly, where obtaining velocity fields would be otherwise cumbersome. The MIR method has been successfully used in PIV studies in complex geometrical arrangements, such as randomly packed spherical beds,[34] wire-wrapped rod bundles,[15] and flow through a mixing-vane spacer grid in a square rod bundle.[35] These studies and several others make use of a wide spectrum of combinations for the solid components and the working fluid such as fluorinated ethylene propylene and water,[36] pcymene and clear polymethylmethacrylate (PMMA or acrylic),[37] mineral oil and quartz,[38] anise oil and epoxy resin,[20] or novel fluids such as combinations of NaCl and ethanol solutions in water with acrylic.[39] For the experiments performed in this study, the combination of clear borosilicate glass (as the solid component) and an organic solvent D-limonene (as the working fluid) was utilized. The benefits of selecting D-limonene as the working fluid are its chemical stability and its low chemical interaction with the facility components. D-limonene and borosilicate glass have optical indices of refraction of 1.4726 and 1.4727, respectively, at a temperature of 23.06 °C (73.5 °F) for a wavelength of 532 nm corresponding to the neodymium-doped yttrium aluminum garnet (Nd:YAG) line.[40] D-limonene has a density, ρ, of 841.9 kg/m^3 and a dynamic viscosity, μ, of 0.907 mPa.s at this temperature condition.

B. 127-pin test section and 3D printed spacer grids

The test section is a prototypical 127 fuel pin assembly arranged in a triangular lattice enclosed in a clear PMMA hexagonal flow channel. 127 annular borosilicate glass rods function as the pins, with an outer diameter of 11 mm, a rod-to-rod pitch of 13.66 mm, and the hexagonal flat-to-flat distance is 165.3 mm. The annular borosilicate rods are filled with D-limonene and are sealed with caps at either end to enable a matching of the optical indices of refraction between solid component and the working fluid. The rod bundle has a total length of 1.5 m. Figure 2(a) shows the experimental configuration used to obtain the two-dimension two-component (2D2C) TR-PIV measurements in the visualization region of the test section. The TR-PIV apparatus consisted of a 20 W continuous laser operating at a wavelength of 532 nm. A Phantom v711 high-speed CMOS camera, adjusted to be incident normal to the laser planes within the test section, was used to capture the raw PIV images. The camera has a pixel size of 20 × 20 μm^2, a 12-bit depth image depth, and a maximum resolution of 1280 × 800 pixels. A 100 mm Nikkor lens was installed on the camera. A filter to remove wavelengths of reflected light, solid component reflections and glare was installed on the lens. The laser thickness was adjusted to be approximately 1 mm wide to fit in the subchannels of interest without interactions with the rods. The camera and the laser were both mounted on three-axis traverse systems to adjust their location by means of a fine and coarse linear translation controller. Figure 2(b) illustrates the implementation the MIR method in the test facility where the rods partially submerged in D-limonene. A clear, unobstructed view through the test section was achieved as compared to air in the unfilled test section region, which is optically opaque. The use of the MIR method enables the capture of PIV images using the aforementioned experimental setup as seen in Fig. 2(c)—a demonstration of the experiments with the laser operational at the near-wall plane of the 127-pin test section.

Hexagonal honeycomb asymmetric spacer grids were installed in the test section, which were 3D printed using stainless steel 304 as the base material—aiding in their structural stability, as well as chemical and operational stability. Three such spacer grids were installed in the rod bundle at axial separations of 500 mm from the previous corresponding spacer grid. The bundle hydraulic diameter, D_h, for this assembly was calculated to be 9.347 mm. For the 127-pin assembly, the primary function of the currently used spacer grid is to enforce consistent rod spacing at defined axial intervals. Figure 3(a) illustrates the 3D-printed spacer grid used for the TR-PIV tests. An additional benefit of these bare honeycomb spacer grid is their function as an obstruction to the working fluid flow, which results in the localized generation of turbulence, where these are installed.

To characterize the wake effects of the spacer grid and the flow passage through the rod bundle, three axial laser vertical planes (VP) were selected, as highlighted in Fig. 3(a). One near-wall plane, VP1, was selected to study the combined wall effects on flow coupled with the complex fluid dynamics interactions past the spacer grid in the vicinity of the near-wall rods. Additionally, one laser plane in the intermediate space of the hexagonal rod bundle, VP2, was selected to study

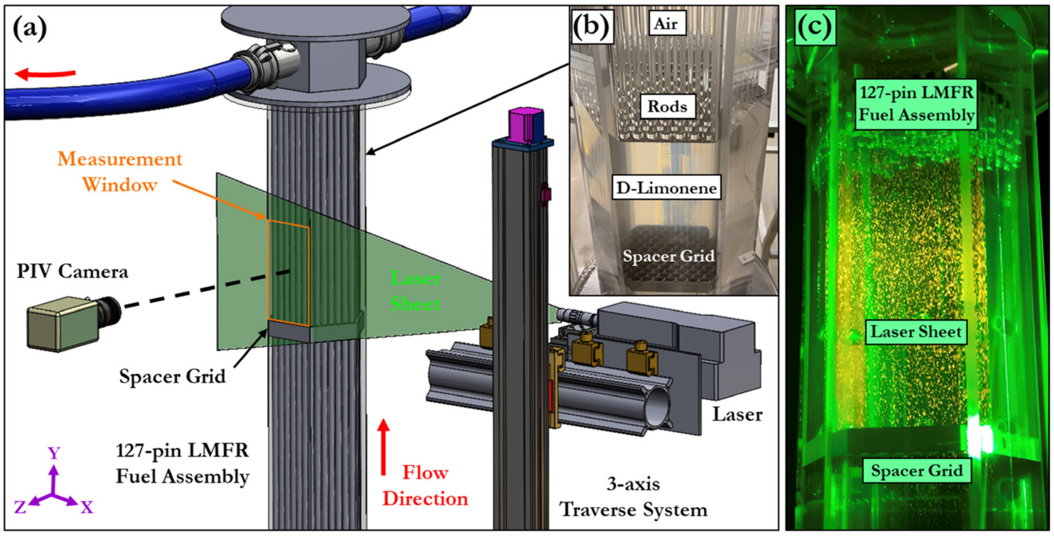

FIG. 2. (a) Experimental setup for TR-PIV measurements in the 127-pin LMFR hexagonal rod bundle. (b) 127-pin bundle MIR test section partially filled with D-limonene, (c) Demonstration of TR-PIV experiments where the fluorescent seeding particles are illuminated by the laser sheet.

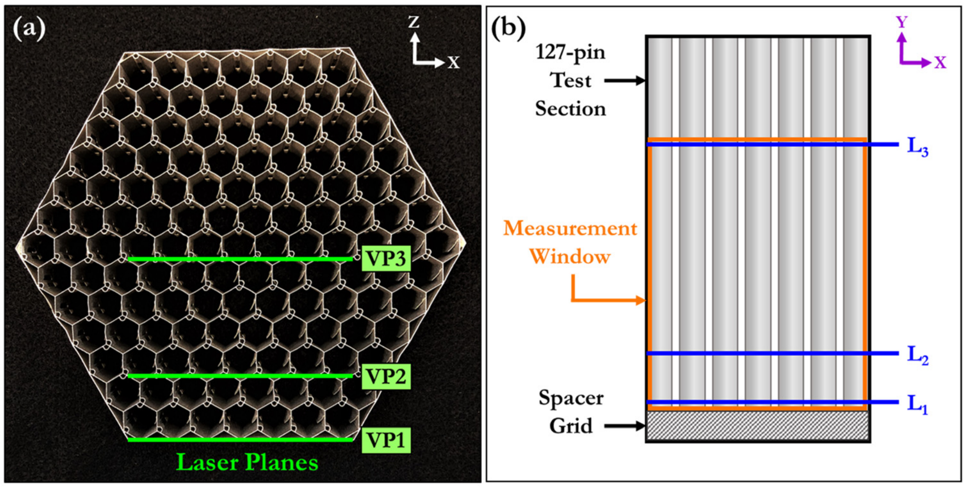

FIG. 3. (a) 3D-printed asymmetric honeycomb spacer grid. The TR-PIV measurement planes (VP1, VP2, and VP3) are highlighted in the figure. (b) Experimental measurement window indicating the lines of interest (L_1, L_2, and L_3) for velocimetry line profiles.

typical flow through the interior subchannels of the rod bundle. A final laser plane near the center of the hexagonal assembly, VP3, was selected to observe how flow patterns differ on progression to the center of the prototypical fuel bundle. The measurement window or the region of interest for PIV image capture is illustrated in Fig. 3(b). Three axial elevations in the measurement window were selected to evaluate velocimetry parameter line profiles—to study the downstream flow effects after encountering the spacer grid. As shown in Fig. 3(b), the line profiles in Sec. IV B 3 were obtained for all three laser planes of interest at: L_1 at an elevation of $Y/D_h = 0.5$, L_2 at $Y/D_h = 2$, and L_3 at $Y/D_h = 10$. The PIV images acquired at the three laser measurement planes allowed full-field visualization in the illuminated measurement region owing to the unobstructed view provided by employing the MIR visualization technique.

Fluid motion in the measurement window was tracked by means of fluorescent orange polyethylene seeding particles with a mean diameter, d_p, of 55 μm, and a density, ρ_p, of 1015 kg/m^3. The fluorescence of the seeding particles resulted in distinct traceability when illuminated by the laser sheet in the measurement planes of interest. To ensure that the particles adequately followed fluid motion, the mean particle response time was evaluated as

$$\tau_p = \frac{d_p^2 \rho_p}{18\mu}. \tag{1}$$

Here, μ is the dynamic viscosity of the working fluid. τ_p was evaluated to be 1.88×10^{-4} s, resulting in an unnoticeable time delay between the particles response to fluid motion. Subsequently, the Stokes number, $Stk = \tau_p/\tau_f$, was evaluated from τ_p and the characteristic timescale, τ_f. For this study, τ_f was evaluated to be 1.38×10^{-1} s, from the bundle hydraulic diameter, D_h, and the bundle bulk flow velocity, $U_0 = 0.6762$ m/s, obtained as detailed in Sec. III. Samimy and Addy[41] and Raffel *et al.*[42] have confirmed that for particle *Stk* below 10^{-1}, the particles closely follow the flow streamlines and reduce measurement errors. For the combination of D-limonene and the orange florescent polyethylene seeding particles, *Stk* was calculated to be 1.36×10^{-3}, confirming the particles' effective tracing of fluid motion in the working fluid for the TR-PIV experimental tests.

III. EXPERIMENTAL METHODOLOGY

The experimental PIV images were acquired at isothermal conditions, which yielded 2D2C velocity distributions in the 127-pin LMFR assembly at a Reynolds number (*Re*) of 6000. For this flow condition, the flow lies in the transition regime, as confirmed from the bare-rod bundle flow transition *Re* predictions by the Pacio-Chen-Todreas Detailed (PCTD) correlation.[43,44] *Re* is defined as

$$Re = \frac{\rho U_0 D_h}{\mu}, \tag{2}$$

where ρ is the density of the working fluid, μ is the dynamic viscosity of the working fluid, U_0 is the rod bundle bulk flow velocity, and D_h is the rod bundle hydraulic diameter. For the given *Re* conditions, U_0 was evaluated to be 0.6762 m/s for the rod bundle and the flow was forced through the test section to maintain this fixed U_0. Steady flow conditions were sustained in the test facility by ensuring a sufficient flow circulation time before performing the experiments at the laser planes of interest. At this steady condition, the number of flow throughs was evaluated to be approximately 4 times through the available flow area within the test section. The seeding particles were premixed with the working fluid in the surge tank, which was circulated through the flow loop, to ensure sufficient mixing and particle density in the working fluid and in the PIV images.

For $Re = 6000$, the PIV camera was operated at 1000 frames per second (*fps*), where $N = 10\,000$ sequential PIV images were utilized for experimental velocimetry statistics, with an interframe time delay of $\Delta t = 0.001$ s. A constant time delay ensured that the statistical PIV parameters were time-resolved. An in-house PIV processing code was utilized to process the experimentally acquired images, similarly utilized in several preceding PIV studies.[15,33,34] The robust phase correlation (RPC) algorithm was used to perform cross-correlation between consecutive image frames, which was proven to reduce bias errors and peak locking effects.[45,46] The velocity vectors were evaluated from the cross-correlation stage and subpixel displacements, obtained using a Gaussian fit.[42] Vector validation was performed using universal outlier detection[47] to identify and replace erroneous vectors resulting from incorrect cross-correlation. The corresponding erroneous vectors were replaced using bicubic interpolation. Three PIV processing passes were performed using grid sizes that were progressively reduced, to ensure correct seeding particle correlation in the PIV images. An initial 128 × 128 pixel interrogation window with 50% overlap was used in the first PIV pass resulting in a grid resolution of 16 × 16 pixels (2.4 × 2.4 mm). For the second PIV processing pass, the interrogation window was reduced to 32 × 32 pixels, returning a grid size of 8 × 8 pixels (1.2 × 1.2 mm). The third and final processing pass then increased overlap to 75% for a final grid spacing of 4 × 4 pixels (0.61 × 0.61 mm). The magnification factor, $\alpha = 0.1515 \pm 0.0013$ mm/pixel, was obtained using the calibration process highlighted by Menezes *et al.*,[32] to convert pixel displacements into physical units in millimeters (mm). For the PIV processing of the experimental data, the number of erroneous vectors that failed the validation process and were interpolated was less than 5% of the total vectors averaged throughout the experimental time. Additionally, cross-correlation using RPC was quantified to be accurate within approximately ±0.1 pixels, as assessed and confirmed by previous studies.[48] A detailed uncertainty analysis based on PIV parameters, instrumentation, and measurement parameters is described in Sec. IV A. Using the aforementioned experimental setup and methodology, the TR-PIV statistics were evaluated and detailed in Sec. IV.

IV. TR-PIV RESULTS

A. Convergence analysis and uncertainty propagation

Several sources of uncertainty for the component-wise velocities from this experimental study have been identified and quantified. First, the streamwise and spanwise instantaneous velocity vector components are computed by

$$u = \alpha\left(\frac{\Delta X}{\Delta t}\right) + \delta u, \tag{3}$$

where α is the magnification factor in m/pixel; ΔX is the displacement between a component-wise correlated image pair, in pixels; Δt is the time delay between image pairs, in s; and δu is the difference between the seeding particle response in the fluid and the actual fluid flow. As the particle Stokes number was determined to be $Stk \approx 10^{-3}$, it is shown that the particles closely follow the flow and the response of the seeding particles, δu, in the fluid can be considered negligible. The uncertainty of the instantaneous velocity vector components was evaluated by propagating the uncertainties of the aforementioned parameters, resulting in

$$\sigma_u = \sqrt{\left(\frac{\Delta X}{\Delta t}\right)^2 \sigma_\alpha^2 + \left(\frac{\alpha}{\Delta t}\right)^2 \sigma_{\Delta X}^2 + \left(\frac{\alpha \Delta X}{\Delta t^2}\right)^2 \sigma_{\Delta t}^2}. \tag{4}$$

The uncertainty in the time delay is given by the camera settings at 1%, or $\sigma_{\Delta t} = 1 \times 10^{-5}$ s. The particle displacement has an uncertainty due to the performance of the RPC algorithm, which was previously quantified at $\sigma_{\Delta X} = 0.1$ pixels.[49,50] Finally, the magnification factor uncertainty was calculated through the calibration process as $\sigma_\alpha = 0.0013$ mm/pixel. Table I lists the normalized propagated measurement uncertainty of the instantaneous velocity components in each plane. The presented uncertainties were normalized by the bulk flow velocity U_0.

TABLE I. Maximum normalized propagated measurement uncertainties, σ_u and σ_v of the instantaneous velocity components in the spanwise (U) and streamwise (V) directions for TR-PIV measurement planes VP1, VP2, and VP3.

Uncertainty	VP1	VP2	VP3
σ_u/U_0	5.1%	4.6%	4.6%
σ_v/U_0	5.6%	5.8%	5.5%

Additionally, the uncertainty of the computed PIV statistical results (i.e., mean velocity, root mean square, and Reynolds stress) is quantified for the presented results, following the method described in Neal *et al.*[51] and implemented by Nguyen *et al.*[11] The normalized standard uncertainty for time-averaged quantities is presented in Table II for the three planes of interest. Since each field of flow is at the same *Re* flow, the statistical uncertainties were observed to possess minimal variation between planes. The near-wall plane, VP1, shows slightly higher uncertainties in the streamwise direction.

It should be noted that the estimation of uncertainty in TR-PIV persists as a prevalent area of research due to the complex interdependencies of the experimental and algorithmic parameters. A diverse set of methodologies are found in the literature, where researchers have sought to resolve this complexity and quantify PIV uncertainties.[33,40,52,53] The uncertainty analysis presented has included major sources of measurement error pertaining to the calibration of the PIV measurement window, the correlation algorithm, the seeding particle properties, the high-speed camera properties, and the standard uncertainties in the time-averaged flow field.

The convergences of the flow statistics were calculated based on an affirmed comparative methodology by several previous PIV studies.[11,54,55] The presented convergence analysis serves as a verification whether a sufficient number of experimental TR-PIV samples were obtained to accurately evaluate the velocimetry parameters. For each experimental plane of measurement, VP1–VP3, a total of $N = 10\,000$ samples were considered. The convergences were estimated as percentages using a progressively increasing number of samples, N_k, for all the grid points, p, in the experimental images. N_k corresponding to $N_1 = 2000$, $N_2 = 4000$, $N_3 = 6000$, and $N_4 = 8000$ snapshots (sequential and beginning from the first snapshot) were selected. The normalized spatially averaged absolute difference values—here, defined as the convergence factor, $\tilde{\epsilon}_{N_k}$—for the aforementioned TR-PIV points for each plane were calculated as

$$\tilde{\epsilon}_{N_k} = \frac{1}{p}\sum_{i=1}^{p}\left|(S_i)_{N_k} - (S_i)_N\right|, \tag{5}$$

TABLE II. Normalized standard uncertainties, ε_U, ε_V, $\varepsilon_{u'_{rms}}$, $\varepsilon_{v'_{rms}}$, and $\varepsilon_{u'v'}$, in percentages for the TR-PIV measurement planes VP1, VP2, and VP3 at $Re = 6000$.

Plane	ε_U/U_0 (%)	ε_V/U_0 (%)	$\varepsilon_{u'_{rms}}/U_0$ (%)	$\varepsilon_{v'_{rms}}/U_0$ (%)	$\varepsilon_{u'v'}/U_0$ (%)
VP1	0.06	0.19	0.04	0.14	0.01
VP2	0.05	0.17	0.04	0.12	0.01
VP3	0.06	0.17	0.04	0.12	0.01

where S_i denotes the first- or second-order statistics in consideration, obtained from the TR-PIV measurements. Figure 4 shows the percentage normalized convergence factor evaluated for the spanwise velocity, U_{avg}; streamwise velocity, V_{avg}; fluctuating spanwise velocity, u'_{RMS}; fluctuating streamwise velocity, v'_{RMS}; and the Reynolds stress, $u'v'$. For each TR-PIV measurement plane, $\tilde{\epsilon}_{N_k}$ was normalized using U_0 for U_{avg}, V_{avg}, u'_{RMS}, and v'_{RMS}, whereas $u'v'$ was normalized using U_0^2.

A considerable decrease in the normalized convergence parameter was obtained by increasing the snapshots from N_1 to N_4. This indicates that convergence was achieved for all experimental measurement planes using the methodology in Sec. III and the selected total number of snapshots, N, for velocimetry parameter estimation. The similarity in $\tilde{\epsilon}_{N_k}$ for a given N_k indicates that the selection of frame rate and grid sizes were selected appropriately. The comparative maximum value of $\tilde{\epsilon}_{N_1} = 0.647\%$ was obtained for V_{avg} at VP2. For N_4, which is closest to N, the normalized convergence factor values for all the considered velocimetry parameters were estimated to be below 0.21%. Following the confirmations from the convergence analysis, all the TR-PIV statistical results were computed using the maximum available snapshots ($N = 10\,000$).

B. Experimental TR-PIV statistical results

In this section, the experimental TR-PIV statistical results are presented, subject to Reynolds flow decomposition for the VP1, VP2, and VP3 at $Re = 6000$. Section IV B 1 highlights the velocity magnitudes and the velocity fluctuation contours, and Sec. IV B 2 presents the contours for the Reynolds shear stress, vorticity, and turbulence kinetic energy. TR-PIV line profiles are presented in Sec. IV B 3 for three axial elevations (L_1, L_2, and L_3) downstream of the spacer grid in the 127-pin hexagonal rod bundle.

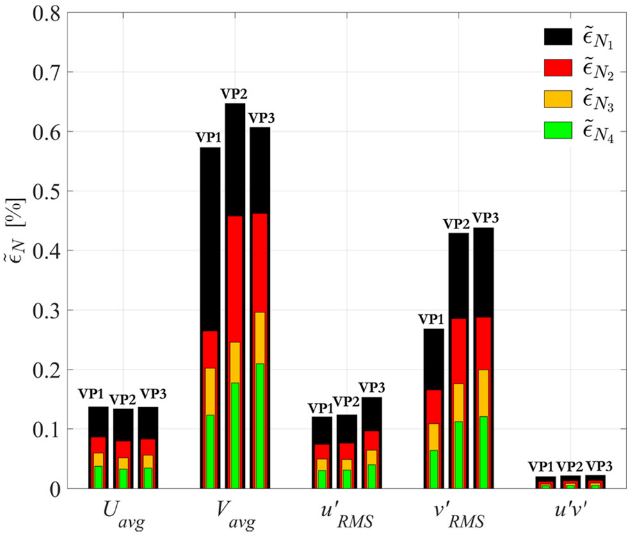

FIG. 4. Convergence assessment using the percentage normalized convergence factor, $\tilde{\epsilon}_{N_k}$, for the first- and second-order TR-PIV statistical results. $\tilde{\epsilon}_{N_k}$ was evaluated for the vertical measurement planes VP1, VP2, and VP3 at $Re = 6000$.

1. Time-averaged velocity magnitudes and root mean squared velocity fluctuations

The normalized time-averaged velocity magnitude fields (U_{mag}/U_0) are shown in Fig. 5(a) for the laser planes VP1, VP2, and VP3 for the 127-pin assembly at Re = 6000. The vectors of U_{mag}/U_0 are depicted in Fig. 5(a), calculated as $U_{\text{mag}} = \sqrt{U_{\text{avg}}^2 + V_{\text{avg}}^2}$, indicating the magnitude and direction of the flow. The streamwise upper limit reported is at $Y/D_h = 10$ since the contours of all discussed parameters show similar behavior downstream of this axial elevation. Strong bypass flow persists in the near-wall edge subchannels, as observed by the higher magnitudes of U_{mag} in VP1. It should be noted that the scale selected for the VP1 results was adjusted to adequately highlight the flow patterns in the near-wall subchannels. The near-wall flow is a consequence of its larger cross-sectional flow area, which allows a larger volume of fluid to pass into VP1. For all the subchannels, alternating regions of higher velocity flow streamlines form due to cross-sectional area constriction. Jet-like flow structures emanate from the spacer grid, which maintain this flow pattern on progressing further downstream of the spacer grid, where the structures at VP1 exhibit wall-jet behavior.[56] Similar flow structures were also found in the 84-rod bundle experiments with staggered spacer grids by Menezes *et al.*[32] The flow in all the laser planes of interest achieves a state close to full flow development at approximately $Y/D_h = 4$, indicating that the turbulence generated due to the spacer grid is highly localized. The interior subchannels shown by VP2 and VP3 show similar U_{mag} contours owing to the similar flow split occurring in the interior subchannels.[57] Furthermore, the maximum U_{mag}/U_0 values were estimated to be 2.033 for VP1, 1.353 for VP2, and 1.387 for VP3.

Figure 5(b) highlights the normalized root mean square (RMS) fluctuating velocity contours in the spanwise direction (u'_{RMS}/U_0). It is immediately observed that the peaks in the contour maps of u'_{RMS} are localized in the regions between the aforementioned jet flow structures. For all the vertical laser planes of interest, VP1–VP3, it can be observed that the peaks in u'_{RMS} demonstrate spanwise periodicity and are below $Y/D_h = 2$. For VP2 and VP3, in the interior subchannels of the fuel assembly, the u'_{RMS} peaks are further constricted up to $Y/D_h = 1$ confirming the restriction of turbulent instabilities in the spanwise direction to the immediate wake of the spacer grid. The effect of the rods on the spanwise velocity was captured in the VP3 measurements above $Y/D_h = 6$, possibly due to a flow volume constriction caused by the rods in the immediate in-plane region. Since the primary function of the 3D printed spacer grid in this rod bundle is primarily to maintain geometrical arrangement, the turbulence generated by the spacer grid shows strong localization. Figure 5(c) compares the normalized streamwise velocity fluctuations (v'_{RMS}/U_0) for VP1–VP3. The fluctuations occur in the shear region where slower moving fluid in the intermittent jet regions interacts with the faster moving fluid. The dominant v'_{RMS} peaks for all the planes of interest demonstrate relative overall symmetry about $X/D_h = 0$, with a comparatively higher symmetry observed at VP1. Streamwise fluctuations due to the rods are apparent from the elongated v'_{RMS} peaks in the interior subchannel laser plane measurements at VP2 and VP3, indicating dominant rod effects on the flow through the 127-pin bundle.

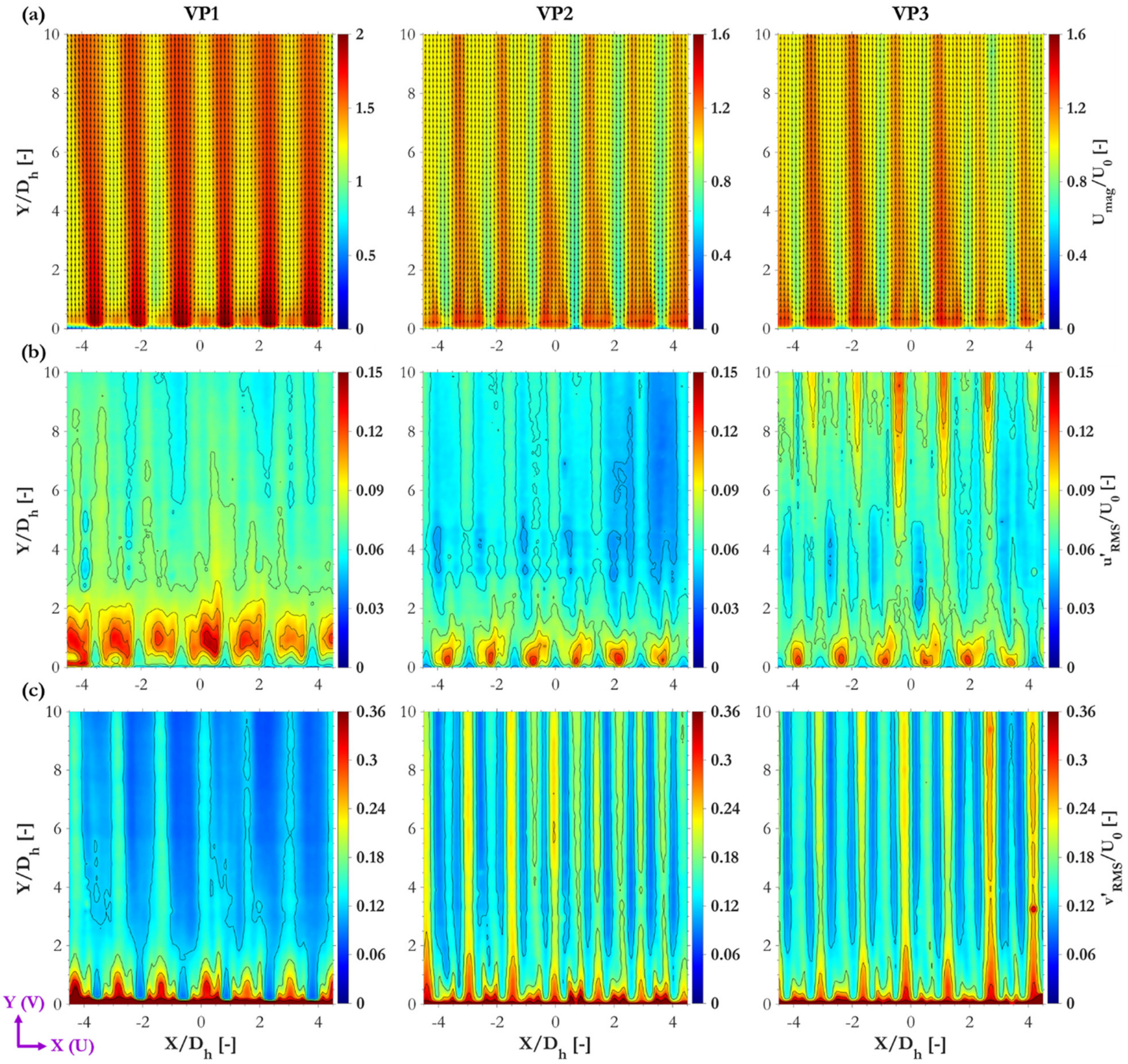

FIG. 5. (a) Normalized time-averaged velocity magnitude (U_{mag}/U_0) contours with superposed velocity vectors, (b) normalized spanwise fluctuating velocity (u'_{RMS}/U_0) contours, and (c) normalized streamwise fluctuating velocity (v'_{RMS}/U_0) contours: for the planes VP1, VP2, and VP3 at $Re = 6000$. The spacer grid is located immediately below $Y/D_h = 0$.

2. Reynolds shear stress, vorticity, and turbulence kinetic energy distributions

The contours of the normalized Reynolds shear stress ($u'v'/U_0^2$) for VP1–VP3 are shown in Fig. 6(a). The Reynolds stress contours characterize the average momentum transfer caused due to turbulent velocity fluctuations. Alternating peaks of high and low intensities are observed in the immediate wake of the spacer grid in the $0 < Y/D_h < 1$ region. The shear stress is strongly influenced by the peripheries of the jet regions, where maximum fluid shear is observed due to the faster moving jet flow structures and the slower moving fluid in the intermediate jet regions, indicating the presence of a fluid–fluid Kelvin–Helmholtz instabilities.[32,33] The intensity of the peaks decreases on progressing inward to the center of the hexagonal assembly, with the strongest magnitudes of the $u'v'$ peaks occurring at VP1 and gradually reducing to lower intensities at VP3. To characterize the presence of fluid structure rotation, the normalized vorticity ($\omega D_h/U_0$) contour maps for the TR-PIV measurement planes were evaluated and presented in Fig. 6(b). The mean velocity vectors for the respective planes are

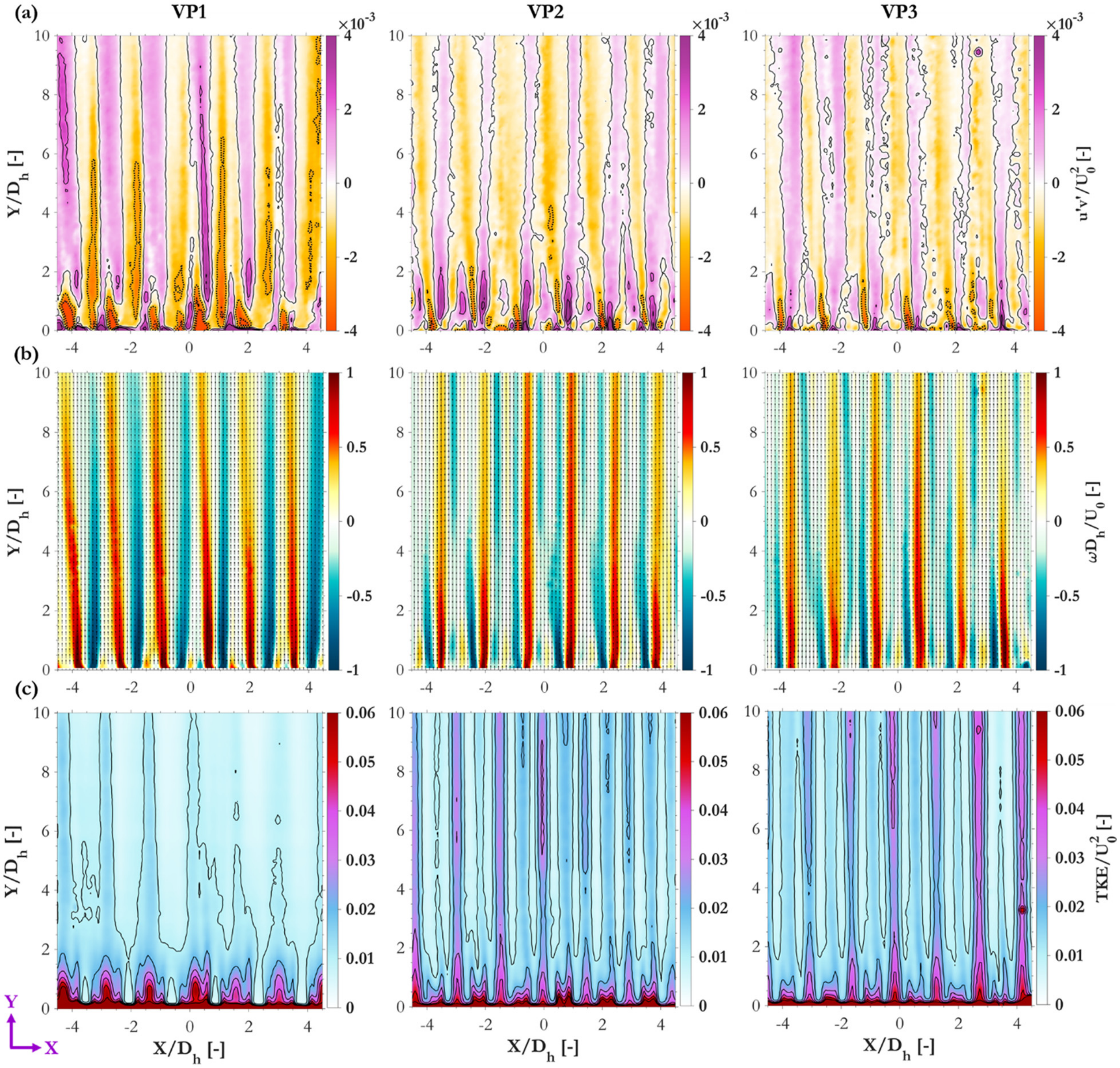

FIG. 6. (a) Normalized Reynolds stress ($u'v'/U_0^2$) color contours, (b) normalized vorticity ($\omega D_h/U_0$) contours indicating the presence of rotation in the shear layers, and (c) normalized turbulence kinetic energy (TKE$/U_0^2$) contours: at $Re = 6000$ for experimental TR-PIV measurement planes VP1, VP2, and VP3.

superposed on the contours of $\omega D_h/U_0$. Figure 6(b) compares the vorticity fields of VP1, VP2, and VP3 to observe the fluid rotation effects due to the spacer grid while moving closer to the center of the bundle. The presence of dominant ω peaks of strong positive and negative intensities is a characteristic feature of the emanating flow in the presented 127-pin assembly for all measurement planes. The boundaries of the jet structures where velocity gradient persists introduce fluid rotation in the peripheral region of the jets, where positive ω indicates counterclockwise fluid rotation and negative values indicate clockwise rotation.

Finally, to quantify the energy possessed by the turbulent fluid motion, the normalized turbulence kinetic energy per unit mass (TKE$/U_0^2$) was evaluated as $\mathrm{TKE} = 0.5 \cdot \sqrt{u'^2_{\mathrm{RMS}} + v'^2_{\mathrm{RMS}}}$. The TKE$/U_0^2$ contour maps are presented for VP1–VP3 in Fig. 6(c). The TKE peaks are once again localized in the regions where the combined effects of u'_{RMS} and v'_{RMS} are the highest. It is noticeable that the TKE production mechanism in all planes are predominantly due to turbulent mixing introduced by the spacer grid functioning as a flow perturbation.[33] Due to the regular geometry of the spacer grid, the TKE spatial contours demonstrate spatial symmetry about $X/D_h = 0$. In the measurement plane VP1, immediate TKE dissipation occurs post the turbulent wake region due to bypass flow accelerating flow development. For VP2 and VP3, the induced fluid instabilities are influenced by the presence of the rods in the constricted flow volume, which illustrate the presence of Kelvin–Helmholtz solid–fluid boundary flow instabilities–causing elongated TKE peaks in the regions where the TKE would otherwise dissipate.

3. Line profiles of TR-PIV statistical results

This section highlights the line profiles of TR-PIV parameters to depict the downstream flow development past the spacer grid in the 127-pin assembly at $Re = 6000$. Important normalized and time averaged first- and second-order parameters such as the spanwise velocity (U_{avg}/U_0), streamwise velocity (V_{avg}/U_0), the RMS fluctuating spanwise component (u'_{RMS}/U_0) and the streamwise component (v'_{RMS}/U_0), the vorticity ($\omega D_h/U_0$), and the turbulence kinetic energy (TKE/U_0^2) were obtained along three axial elevations. In the comparisons, U_{avg}, V_{avg}, u'_{RMS}, and v'_{RMS} were normalized by the bulk flow velocity U_0, whereas ω was normalized using D_h/U_0, and TKE by U_0^2. The first elevation is located at line L_1 ($Y/D_h = 0.5$, $-4.5 < X/D_h < 4.5$) in close proximity of the spacer grid, the second is at line L_2 ($Y/D_h = 2$, -4.5 $< X/D_h <$ 4.5), and the final is at line L_3 ($Y/D_h = 10$, $-4.5 < X/D_h < 4.5$), which is the furthest downstream of the spacer grid. Figure 7(a) presents U_{avg}/U_0, and Fig. 7(b) shows V_{avg}/U_0 for the aforementioned axial elevations for each vertical plane of measurement, VP1–VP3. The U_{avg} line profiles capture the spanwise outward flow originating from each jet structure, which was found to be of highest intensity for VP1, with lower but similar intensities captured for VP2 and VP3. The bypass effects due to the wall gap in the near-wall subchannels yield higher streamwise flow velocity peaks seen in the V_{avg} line profiles at VP1, followed by the lower yet similar intensities for nominal flow at the subchannels represented by VP2 and VP3. The presence of local peaks in both U_{avg} and V_{avg} reduces when progressing from L_1 to L_3, indicating local fluid acceleration immediately past the spacer grid followed by progressive deceleration further downstream. The similarity of the velocity profiles at VP2 and VP3 further confirms the validity of the assumption of similar treatment of velocity profiles in interior subchannels, by the Upgraded Cheng and Todreas Detailed (UCTD)[57] and Pacio-Chen-Todreas Detailed (PCTD)[43,44] predictive correlations for bare hexagonal rod bundles.

The strong immediate turbulence generated in the downstream vicinity of the spacer grid results in dominant u'_{RMS} [Fig. 8(a)] and v'_{RMS} [Fig. 8(b)] peaks and at L_1 for VP1–VP3. For both u'_{RMS} and v'_{RMS}, the fluctuations stabilize as these face downstream decay.[33] The dominant turbulence effects up to $Y/D_h = 2$ yield the peaks and valleys of turbulent fluctuations in v'_{RMS}, which stabilize, as observed in the v'_{RMS} profiles at L_2 and L_3. In the interior subchannels portrayed at VP3, the rod effects cause increased spanwise fluctuations downstream of the spacer grid at L_3, as also observed in the contour maps in Fig. 8(b). Flow development was confirmed past $Y/D_h = 4$, based on the stabilization of the line profiles of U_{avg}, V_{avg}, u'_{RMS}, and v'_{RMS}.

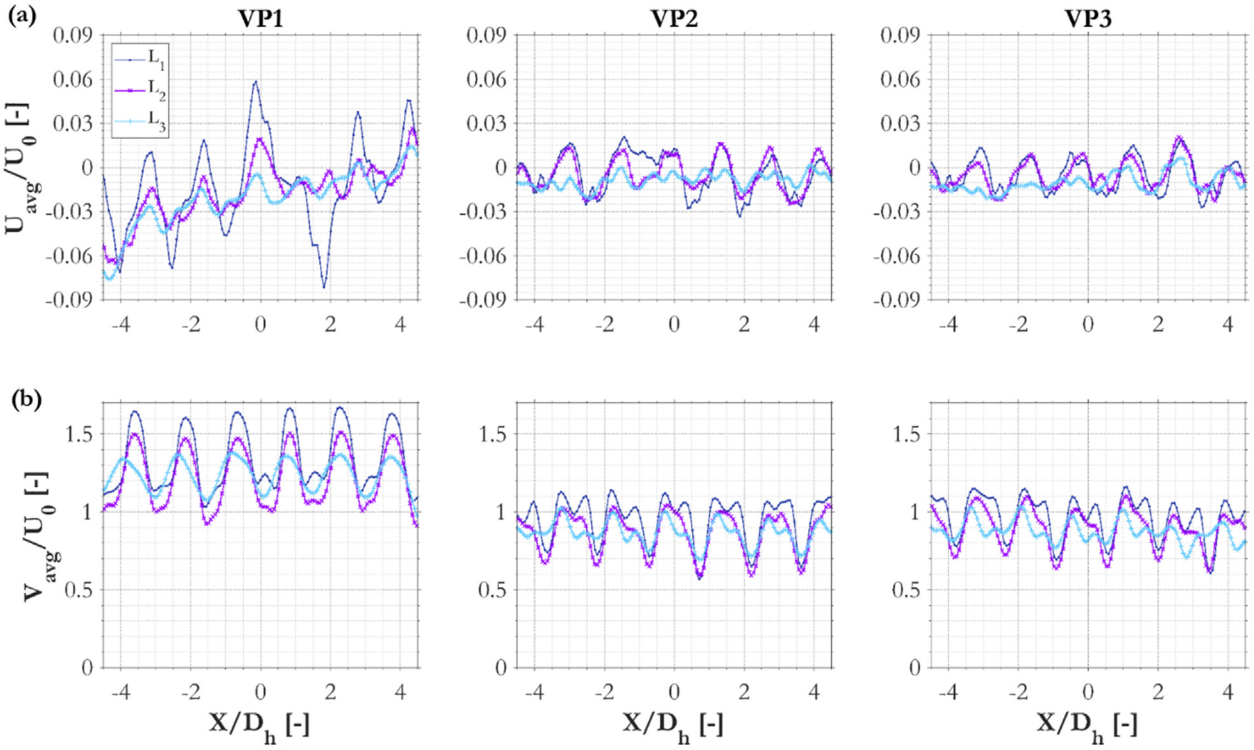

FIG. 7. TR-PIV sub-channel-dependent line velocity profiles indicating downstream flow effects at L_1 ($Y/D_h = 0.5$), L_2 ($Y/D_h = 2$) and L_3 ($Y/D_h = 10$) past the spacer grid (at $Y/D_h = 0$) for the: (a) normalized average spanwise velocity (U_{avg}/U_0) and (b) normalized average spanwise velocity (V_{avg}/U_0).

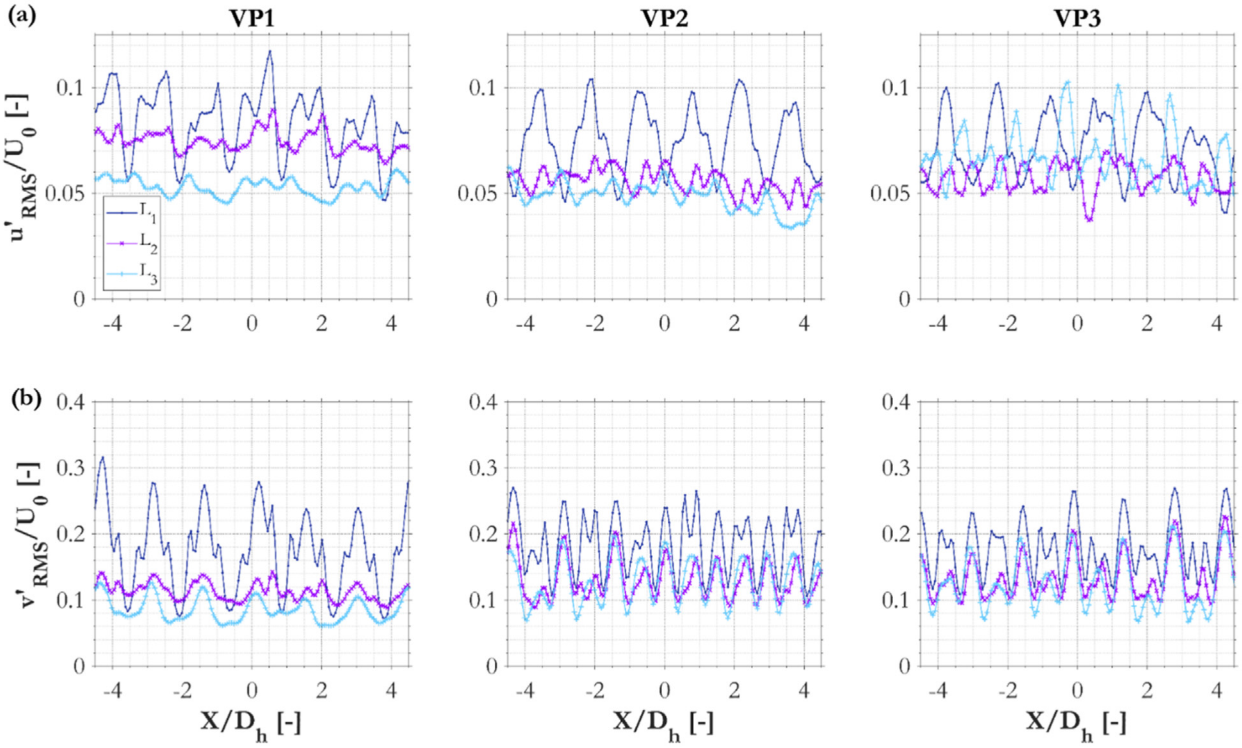

FIG. 8. Line profiles of the (a) normalized spanwise velocity fluctuations (u'_{RMS}/U_0) and (b) normalized streamwise velocity fluctuations (v'_{RMS}/U_0): at L_1 ($Y/D_h = 0.5$), L_2 ($Y/D_h = 2$), and L_3 ($Y/D_h = 10$) past the spacer grid for VP1–VP3.

The velocity gradients in the interspatial region between the jet structures cause fluid shear and rotation displaying alternating positive and negative intensities in the normalized vorticity ($\omega D_h/U_0$) line profiles [Fig. 9(a)], which dissipate downstream. The averaged local fluid rotation in the shear and rotation layers occurs due to the velocity gradient in these regions.[58] As observed in the previously discussed line profiles for average velocity and velocity fluctuation components, the vorticity also demonstrates a similarity downstream at L_3 for planes VP1, VP2, and VP3. In Fig. 9(b), the decay of the normalized TKE (TKE/U_0^2) to the developed values at L_3 is observed for these planes of measurement, with the regions of highest turbulence demonstrating peaks in intensities. The presented line parameters in this section for the first- and second-order velocimetry parameters are imperative for CFD model validation and development. Subsequently, the spacer grid design and geometry for such rod assemblies can be optimized to enhance performance parameters such as turbulence, heat, and momentum transport.

C. Spatial–temporal cross-correlation analysis

In this section, the transition regime flow downstream of the spacer grid was studied using two-point spatial–temporal cross-correlations. Cross-correlation analysis provides insight into the vortical structures present in the flow in different measurement regions in the bundle, downstream of the spacer grid. This analytical method was successfully implemented in previous experimental PIV rod bundle studies by Menezes *et al.*,[15] Matozinhos *et al.*,[33] and Nguyen *et al.*[10] The spatial–temporal cross-correlation is computed by the following equation:

$$R_{vv}(x,\eta,\tau) = \frac{\langle v'(x,t)\cdot v'(x+\eta,t+\tau)\rangle}{\sqrt{\langle v'^2(x,t)\rangle}\sqrt{\langle v'^2(x+\eta,t+\tau)\rangle}}, \qquad (6)$$

where R_{vv} is the spatial–temporal cross-correlation of the streamwise fluctuating velocity vector v', x is the spatial reference point 2D vector, τ is the temporal time delay, and η is the spatial separation vector from the reference point measurement.[59] The same procedure can be performed to compute the cross-correlation of the spanwise velocity fluctuations, R_{uu}. To compute two-point spatial cross-correlations, the time delay is set to zero, $\tau = 0$. This selection reveals the spatial extent of correlated regions and characterizes the local coherent structures and turbulent mixing. For the inclusion of a time delay, the correlation of the fluctuating velocity in one spatial direction is characterized across time. This helps to provide further detail on the local convection velocity and temporal extent of vortical structures that result in correlated velocity fluctuations.

1. Two-point spatial cross-correlation distributions

The two-point spatial cross-correlations of the streamwise and spanwise fluctuating velocities are depicted in Fig. 10 for the wall subchannel (VP1) and two interior subchannels (VP2 and VP3). Nine reference points are presented to characterize each measurement plane,

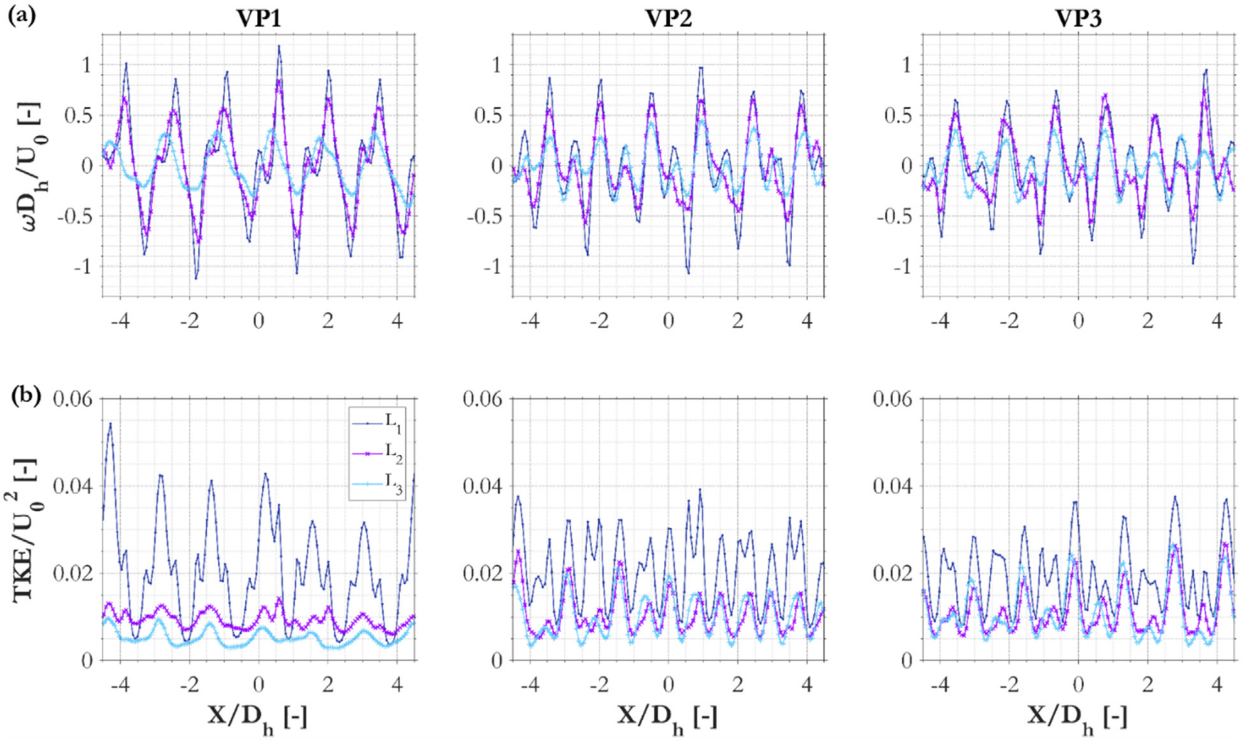

FIG. 9. Evolution of the (a) normalized vorticity ($\omega D_h/U_0$) and normalized turbulence kinetic energy (TKE/U_0^2) (b) at L_1 ($Y/D_h = 0.5$), L_2 ($Y/D_h = 2$), and L_3 ($Y/D_h = 10$) past the spacer grid for VP1–VP3 at $Re = 6000$ in the 127-pin hexagonal rod bundle.

located at $X/D_h = [-3, 0, 3]$ and $Y/D_h = [2, 5, 8]$, which were representative of the spatial cross-correlation contours in their immediate spatial vicinities. The spatial extent of the correlated regions in the X and Y directions was largely similar due to low interference from the bare rod bundle. For the bare hexagonal spacer grid, the transitional nature of the flow at $Re = 6000$ results in almost isotropic flow behavior – also confirmed by the symmetry of the highly correlated regions on progressing inward toward the center of the 127-pin fuel bundle from VP1 to VP3. Lightly correlated regions indicate some deformation in the streamwise direction of the R_{vv} correlations. Meanwhile, R_{uu} correlations in the interior subchannel of VP2 [Fig. 10(b)] exhibited weak alternating peaks due to local vortical motion downstream of the spacer grid at $Y/D_h = 5$ and $Y/D_h = 8$. As shown by the velocity magnitude profiles in Fig. 5(a), these points in VP2 lie along a velocity gradient, which explains the presence of a small local recirculation regions with vortices along the shear layer between fast and slow fluid flow.

2. Two-point spatial–temporal cross-correlation

Spatial–temporal cross-correlations of the streamwise fluctuating velocity R_{vv} were computed for two reference points in each plane, as depicted by the color contours in Fig. 11. Reference point $P1$ is located at $(X/D_h, Y/D_h) = (1.0, 5.0)$, normalized by the hydraulic diameter D_h, while $P2$ is located closer to the spacer at $(X/D_h, Y/D_h) = (1.0, 1.5)$. In the contour plots, the horizontal axis is the time delay, $\tau U_0/D_e$, normalized by the eddy turnover time, D_e/U_0 in s. The eddy diameter, D_e, was estimated by the radius of the circle subscribed in the subchannel gap between fuel rods.[5] Meanwhile, the vertical axis is the normalized axial height above the spacer grid, Y/D_h, inside the 127-pin rod bundle. The cross-correlations reach a unity value when the time delay and separation distance from the reference points are zero (i.e., $\tau = 0$ and $\eta = 0$). As separation distances and time delay increases, the correlation between streamwise velocity fluctuations decreases. As depicted in Fig. 11, the spatial correlation at each time delay is relatively small. However, the spatial–temporal correlated regions reveal interactions between traveling vortices that persist with time delays from 10 to 50 ms. In VP1 and VP3, the interactions at $P1$ are long-lived due to the homogenization of turbulent flow downstream of the spacer. This is not the case in VP2, because $P1$ is closer to the boundary of fast and slow velocity streamlines, which results in rapid decay of traveling vortices. Additionally, the short-lived correlations near the spacer at $P2$ indicate rapid decay of the secondary flow structures.

The slope of the spatial–temporal cross-correlation is known to represent the convection velocity U_c, or average traveling speed of large and small vortices. The convection velocity was quantified using linear regression and normalized by the bulk velocity, as denoted by the dotted lines and annotations in Fig. 11. The local velocity magnitude alternates between fast and slow streamlines. This has a noticeable effect on the convection velocity, resulting in a sinusoidal variation in the convection velocity along the lateral direction in the

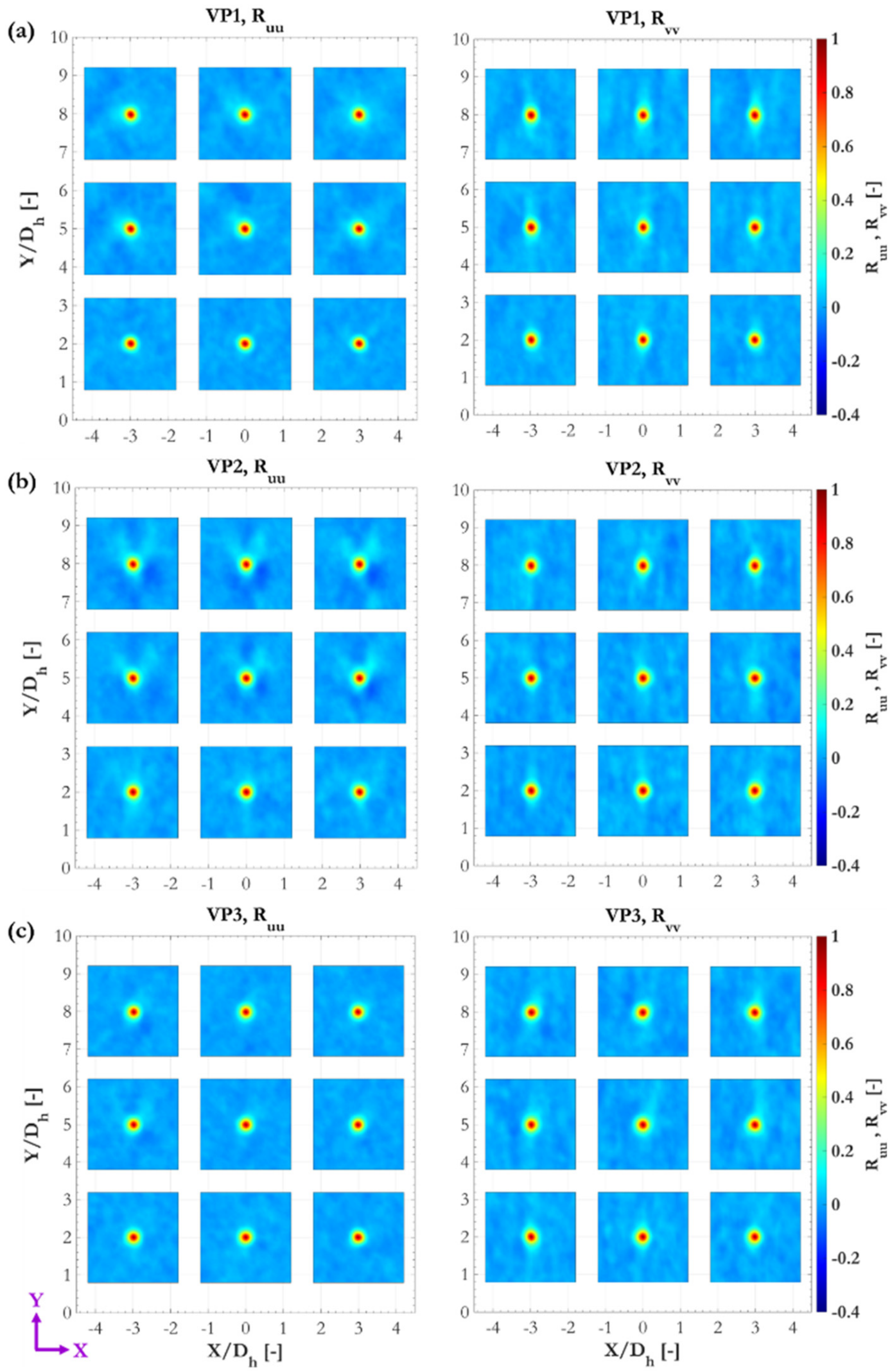

FIG. 10. Two-point spatial cross-correlations of the TR-PIV spanwise fluctuating velocities (R_{uu}) and streamwise fluctuating velocities (R_{vv}) for several reference points in the measurement planes: (a) VP1, (b) VP2, and (c) VP3.

measurement window. In Table III, the maximum, average, and minimum convection velocities were identified for two heights above the spacer grid in each plane. It is shown that the near-wall flow has higher convection velocities for fast and slow streamlines due to the effect of bypass flow. Interestingly, the height above the spacer grid from 1.5 hydraulic lengths to 5.0 hydraulic lengths did not have a significant effect on the average convection velocity. The spatial–temporal results for VP2 (Fig. 11) demonstrate the velocity gradient between a fast and slow streamline region. The normalized convection velocities in VP2 are therefore closer to the mean values computed in Table III, whereas

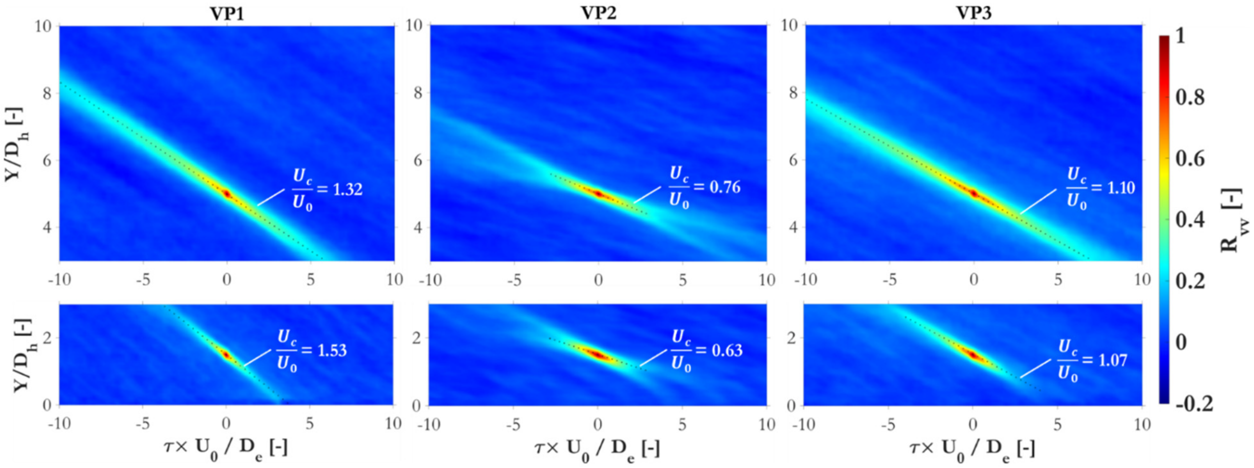

FIG. 11. Contours of the spatial–temporal velocity cross-correlations for the streamwise component (R_{vv}) for point P_1 at $(X/D_h,\ Y/D_h) = (1.0,\ 5.0)$ and P_2 at $(X/D_h,\ Y/D_h) = (1.0,\ 1.5)$. The slope of the spatial–temporal cross-correlation extents yields the turbulent eddy convection velocity, U_c. The normalized convection velocities (U_c/U_0) are highlighted in the figure.

the selected points in VP1 and VP3 lie in fast streamlines with convection velocities comparable to the maximum values in Table III.

V. DYNAMIC MODE DECOMPOSITION FOR THE TR-PIV RESULTS

A. Dynamic mode decomposition overview

While time-averaged flow parameters describe the mean flow of the 127-pin fuel assembly, it is imperative to analyze the turbulent flow structures in the immediate vicinity of the spacer grid to identify important characteristics of turbulence behavior. Such flow structures, which may recur and contribute to fluid momentum transport, are defined as coherent structures.[60] Distinguishing dominant flow features, associated with the interrelated fluid dynamics and heat transport mechanisms, allow an augmented understanding into the optimization of spacer grid design and rod bundle geometry. Many flow decomposition methodologies persist in the literature to achieve the aforementioned objectives.[61] The proper orthogonal decomposition (POD) is one such widely used mathematical methodology employed to extract statistically dominant flow structures. A derivative of the Karhunen–Loeve decomposition, POD, provides a low-dimensional basis of the flow to return spatial decompositions of the most energy containing flow structures.[62] These spatial fields, or modes, are associated with their orthogonal temporal evolution coefficients to yield an encapsulated overview of an investigated flow field.[63] Despite its benefits to detail energetic flow structures associated with their time evolution, important time dynamics information may be lost due to the methodology of associating a specific spatial mode with its respective overall and orthogonal time evolution. Furthermore, in the POD algorithm, the temporally averaged spatial correlation matrix that produces second-order statistics introduces an information loss of possibly important spatiotemporal coherent structure formations.[64]

TABLE III. Normalized convection velocities (U_c/U_0) for two streamwise elevations $Y/D_h = 1.5$ and $Y/D_h = 5.0$ downstream of the spacer grid. The maximum, average, and minimum U_c/U_0 values are summarized for VP1, VP2, and VP3.

Location	Parameter	VP1	VP2	VP3
$Y/D_h = 1.5$	$(U_c/U_0)_{max}$	1.45	1.08	1.13
	$(U_c/U_0)_{avg}$	1.13	0.71	0.76
	$(U_c/U_0)_{min}$	0.66	0.38	0.46
$Y/D_h = 5.0$	$(U_c/U_0)_{max}$	1.58	1.11	1.12
	$(U_c/U_0)_{avg}$	1.09	0.70	0.73
	$(U_c/U_0)_{min}$	0.56	0.30	0.37

An alternative mathematical methodology to extract important temporal and frequency related information is Dynamic Mode Decomposition (DMD), which is a spatiotemporal dimensionality reduction technique based on Koopman analysis.[65] Initially introduced to the fluid dynamics community by Schmid,[66] DMD is effective at providing a linear basis, or approximation, for complex nonlinear flow fields (such as transition and turbulent regime flows). DMD is especially useful since it provides a transient quantification of the spatial and temporal decomposition of dominant flow structures, along with their stability, the rate of growth, and oscillation frequencies of the respective spatially decomposed modes. As compared to POD whose orthogonality denotes spatial independence of the decomposed modes, DMD modes are spatially orthogonal with associated temporal frequencies that evolve independently as time progresses, therefore also temporally orthogonal.[67] Several variations of the DMD methodology have been developed since its inception, as particularized in the works of Kutz *et al.*,[68] Erichson *et al.*,[69] and Jovanovic *et al.*,[70] among others.[71,72] The DMD analysis technique utilized in this experimental investigation is the Exact DMD method due to the TR-PIV data being real-valued and separated by a constant time interval—detailed by Kutz *et al.*[73] and briefly described in Sec. V B. Experimental TR-PIV snapshots at $Re = 6000$ for the near-wall vertical plane VP1 were decomposed into its spatial modes and temporal dynamics—which return important mode growth and oscillation information as quantified frequencies.

B. Dynamic mode decomposition methodology

For the TR-PIV data at the near-wall plane VP1, a total of $N = 10\,000$ distinct instantaneous vorticity snapshots were considered for the DMD analysis at an *fps* of 1000. The snapshots were arranged in two matrices, ω and ω', where the individual snapshots are separated by a constant time interval, $\Delta t = 0.001$ s, as

$$\omega = \begin{bmatrix} | & | & | & | \\ \omega_1 & \omega_2 & \dots & \omega_{N-1} \\ | & | & | & | \end{bmatrix}, \quad \omega' = \begin{bmatrix} | & | & | & | \\ \omega_2 & \omega_3 & \dots & \omega_N \\ | & | & | & | \end{bmatrix}. \tag{7}$$

A locally linear approximation is estimated by performing the singular value decomposition (SVD) using a truncated number of modes, k ($k < N$), to provide a reduced yet meaningful reduced-order model of the near-wall flow in the edge subchannels of the 127-pin bundle

$$\omega \approx U\Sigma V^*, \tag{8}$$

where U is the left singular matrix, Σ is the scaling matrix, and V^* is the conjugate transpose returning the left singular values of ω. A determining factor of the effectiveness of SVD for this flow system is to obtain a sharp decrease in the singular values to zero, as highlighted in Sec. V C 1. The linear approximation of the best-fit linear operator, A, is then estimated to relate the matrices as $\omega' \cong A\omega$, given by

$$\begin{aligned} A &= \omega'\omega^\dagger, \\ A &= \omega' V\Sigma^{-1}U^*, \end{aligned} \tag{9}$$

where $\omega^\dagger$ is the Moore–Penrose pseudoinverse of ω, which provides the least squares solution for systems which may be overapproximated or underapproximated depending on the number of snapshots used to describe a flow system.[74] As previously stated, for computational efficiency and to obtain a comprehensive reduced-order model, the modes were truncated to an $k \times k$ projection of the matrix A, as per

$$\tilde{A}_{k\times k} = U^*\omega' V\Sigma^{-1}. \tag{10}$$

Here, $\tilde{A}_{k\times k}$ is the low-dimensional linear approximation and its eigendecomposition returns the eigenvectors, W, and its usually complex valued eigenvalues, λ, as seen in

$$\tilde{A}W = W\lambda. \tag{11}$$

Finally, the exact DMD modes, Θ, are reconstructed from the decomposition of the matrix A, calculated by

$$\Theta_{k\times k} = \omega' V\Sigma^{-1}W. \tag{12}$$

The eigenvectors in the truncated space, $\Theta_{k\times k}$, describe the most-important spatially decomposed flow structures and its corresponding eigenvalues, obtained from λ, relay important information pertaining to the temporal dynamics of the respective modes. On converting the eigenvalues to the phase space as per $\Lambda_n = \log(\lambda_n)/\Delta t$, the real values of Λ, $\Lambda_{n,r}$, provide the growth or decay rate of the given mode, n; and the imaginary values, $\Lambda_{n,i}$, yield their respective oscillation frequencies – detailed further in Sec. V C 2.

C. Dynamic mode decomposition results

1. DMD mode stability analysis

The results of the DMD analysis on the vorticity fields utilizing the aforementioned methodology are presented in this section for the VP1 experimental plane at $Re = 6000$. The number of truncated modes selected was $k = 150$. Figure 12 illustrates the DMD singular values and the cumulative singular value spectra. A sharp decrease in the singular values, as described in Sec. V B, was observed for the selected k, with the largest representation described in mode $n = 1$. This demonstrates that the TR-PIV data were adequately reduced to a low-dimensional basis and the selected k was sufficient in describing the spatial–temporal flow behavior for VP1 in the 127-pin assembly. For subsequent analysis, it should be noted that the low-order modes $n = 1, 2, 3, 5, 6$, and 8 were studied because these modes were observed to represent a majority of the dominant flow characteristics, which are detailed in this section.

Owing to DMD's similarity to the Arnoldi algorithm allowing its representation in the Krylov subspace, the eigenvalues are equivalent to the Ritz values—whose stability characteristics can now be quantified.[75,76] The Ritz value spectrum of the DMD eigenvalues, λ, was plotted in Fig. 12(b) to analyze the mode stability characteristics of fluid flow immediately after encountering the spacer grid at VP1. In this comparison of the real component of the eigenvalues, λ_r, to the imaginary component, λ_i, the modes with eigenvalues on the unit circle denote neutral stability, whereas modes within the unit circle signify stable decay and the modes with eigenvalues outside the unit circle would signify unstable growth or instability.[74]

As appreciated in Fig. 12(b), Mode 1 lies in near proximity within the unit circle implies that the most dominant mode indicates inherent mode stability, and its value below 1 implies that Mode 1 is slightly damped. To study the stability characteristics of the low-order modes which follow ($n = 2, 3, 5, 6$, and 8), their position on the Ritz value spectrum was analyzed, as highlighted by the colored points in Fig. 12(b). Damped and increasingly decaying behavior was observed for all the aforementioned modes—a consequence also observed for certain modes in the study by Schmid *et al.*[66] for jet flow between two cylinders—implying important flow characteristics reduce in intensity as time progresses. All the modes, including the higher-order modes, demonstrated convergence with increasing decay rates, owing to their positions within the unit circle on the Ritz value spectrum.[77]

2. Mode frequency and PSD analysis

In addition to providing critical mode stability characteristics, the DMD eigenvalues can also be used to characterize the temporal decay rates and oscillation frequencies of the relevant modes, which describe the fluid dynamics of the system. To quantify these decay rates and temporal frequencies of each mode, the eigenvalues were converted to the temporal space, as

$$\Lambda_n = \log(\lambda_n)/\Delta t, \tag{13}$$

where the real component of Λ_n for a given mode n, $\Lambda_{n,r}$, quantifies the decay rates for the modes at the near-wall plane in Hz, and the imaginary components, $\Lambda_{n,i}$, provide the frequency of mode oscillation in Hz. Figure 13(a) presents the DMD spectrum for modes $1 \le n \le 150$.

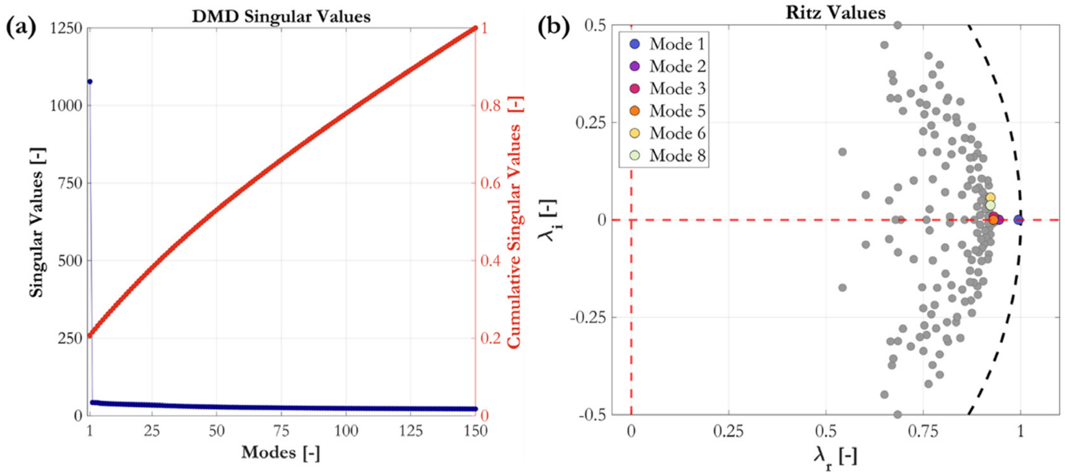

FIG. 12. DMD analysis of the vorticity fields at the near-wall plane (VP1) for $Re = 6000$ highlighting the (a) DMD singular value spectra and the DMD cumulative singular value spectra; and (b) Ritz value DMD eigenvalue stability analysis demonstrating that all DMD modes for VP1 lie within the unit circle and are stable yet decaying.

The oscillatory behavior of the modes is also reported using $\Omega_{n,i}$ in rad/s to comprehend their cyclical periodicities, where $\Omega_n = \log(\lambda_n)/2\pi\Delta t$. Mode decay is a dominant phenomenon observed for all DMD modes at VP1, represented by the exclusively negative $\Lambda_{n,r}$ values. The most stable and least decaying mode is the dominant mode at $n = 1$, which as seen in the spatial mode representation in Fig. 14, resembles mean vorticity [Fig. 6(b)]. The decay rates (represented by the negative $\Lambda_{n,r}$ values) and the oscillation frequencies ($\Lambda_{n,i}$ values) for the selected lower-order modes are summarized in Table IV.

Additionally, the power spectral density (PSD), $\|\Theta_n^\omega\|^2$, of the DMD spatial modes, Θ_n^ω, was evaluated and normalized based on the cumulative L_2 norm, $\sum_{n=1}^{k} \|\Theta_n^\omega\|^2$ ($k = 150$) as the cumulative represents the total energy content of the decomposed system. In Fig. 13(b), the relevant low-order dynamic modes are highlighted by individual colors. Mode 1 represents the highest system energy content, which signifies steady characteristics representing system flow dynamics with minimal decay.[78] For $n > 2$, $\|\Theta_n^\omega\|^2$ indicates the smaller and similar contribution of these modes to the overall flow dynamics. The inlayed plot in Fig. 13(b) also illustrates the temporal phase progression, in rad, for $1 \leq n \leq 30$. The phase angle and delay of $n = 1$, 2, and 5 have zero values, hence are standalone non-oscillatory flow representations, whereas phase delays for θ_3–θ_4 of 0.017 rad, θ_6–θ_7 of 0.123 rad, and θ_8–θ_9 of 0.081 rad indicate the temporal lag between adjacent modes equivalent symmetric real eigenvalue components and non-zero conjugate imaginary components.[74] The presented DMD PSD analysis provides a means for determining the energy content-dependent mode relevance, which is important to identify relevant modes, which characterize flow behavior.

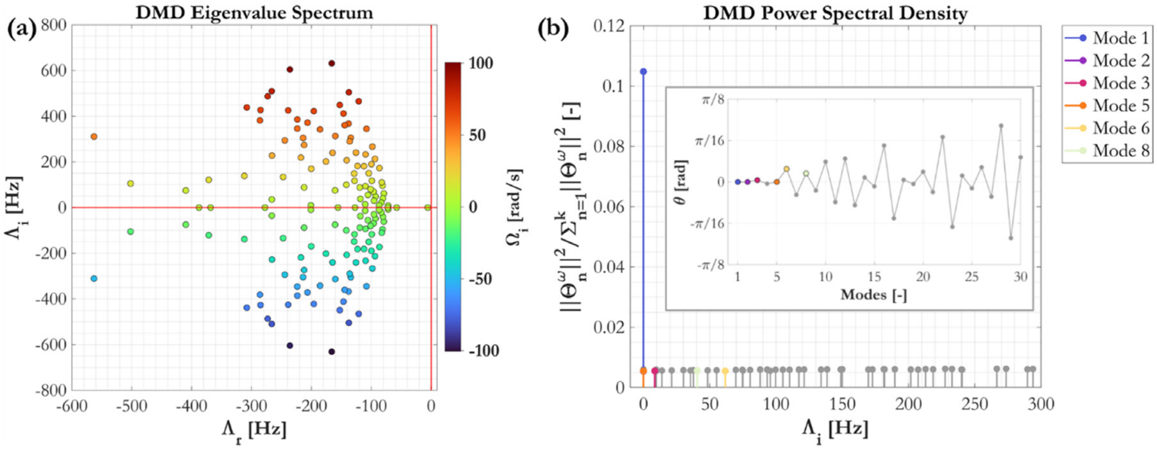

FIG. 13. Near-wall plane (VP1) DMD frequency and PSD analysis at $Re = 6000$ showing the: (a) DMD eigenvalue spectrum quantifying the decay rates ($\Lambda_{n,r}$) and mode oscillation frequencies ($\Lambda_{n,i}$) in Hz. The colorbar indicates the magnitude of mode oscillation frequencies, $\Omega_{n,i}$, in rad/s; and the (b) DMD normalized power spectral density with the oscillation frequency spectra (inlayed figure).

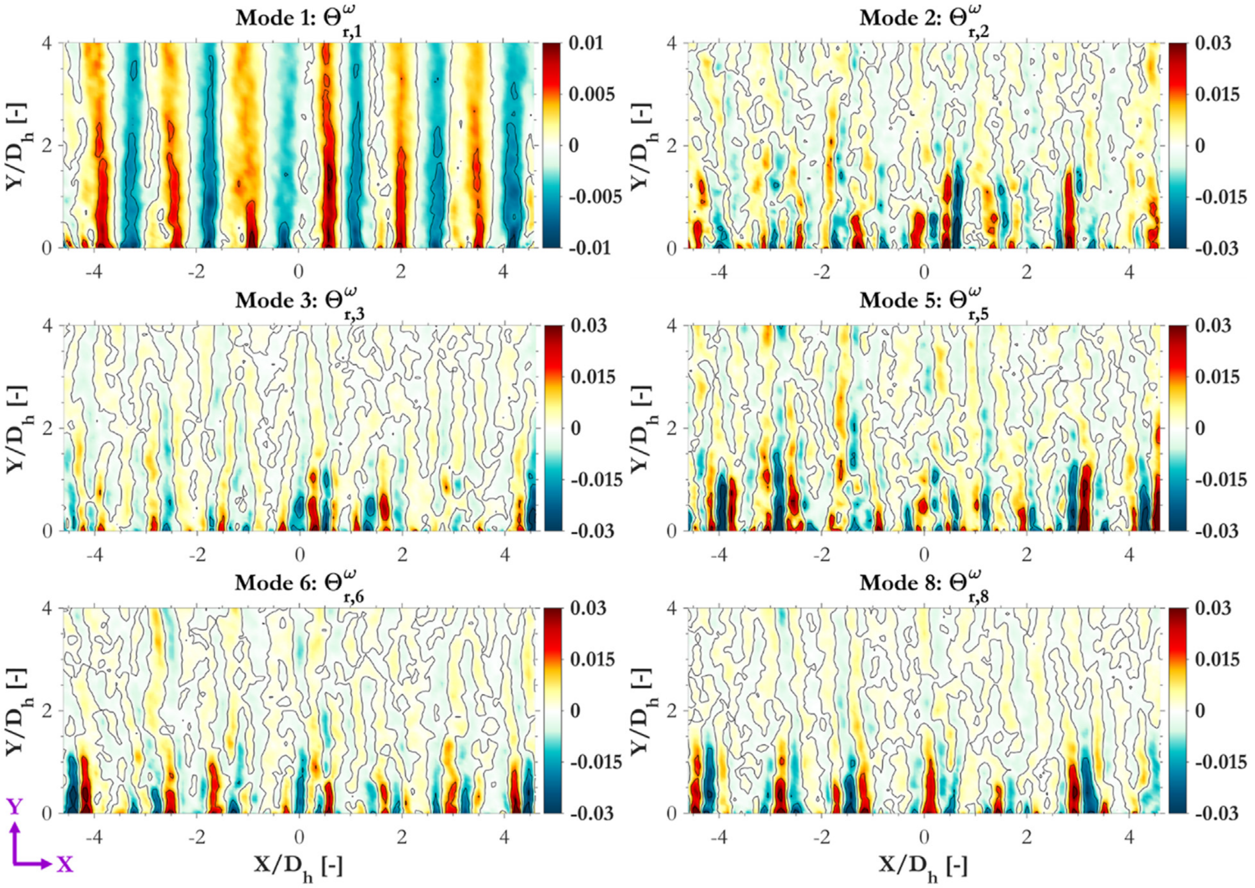

FIG. 14. Real-valued exact DMD lower-order vorticity spatial modes, $\Theta^{\omega}_{r,n}$, for $n = 1$, 2, 3, 5, 6, and 8 at the near-wall plane VP1 for $Re = 6000$ indicating coherent structures formations and the localization of spacer grid induced turbulence.

2. Dynamic mode decomposition spatial modes

The temporal and stability characteristics of the DMD modes provide important information pertaining to their presence, persistence, and oscillations. The spatial modes, Θ_n, provide a visual representation of the mathematically dominant and energy-containing flow structures in the near-wall plane of the 127-pin LMFR fuel assembly, due to the flow instabilities arising from the presence of the spacer grid and the rods. It should be noted that the spatial modes occur as complex conjugates for non-zero temporal frequencies. Here, the real-valued spatial fields for the vorticity, $\Theta^{\omega}_{r,n}$, denote the spatially dominant coherent structure formations, while their complex counterparts, $\Theta^{\omega}_{i,n}$, denote the oscillatory spatial response.[79] For the presented DMD analysis of ω at VP1, the $\Theta^{\omega}_{r,n}$ fields where chosen for investigation in the highlighted modes due to the relative similarity captured between $\Theta^{\omega}_{r,n}$ and $\Theta^{\omega}_{i,n}$. It should also be noted that single, unique representations of the spatial flow effects for $n = 1$, 2, and 5 are described by their corresponding $\Theta^{\omega}_{r,n}$ fields due to the nonexistence of a temporal oscillation frequency [Fig. 13(b)]. Conversely, only the lower-order modes $n = 3$, 6, and 8 are shown since their real-valued part is symmetric with their respective conjugates (occurring for $n = 4, 7$, and 9).

TABLE IV. DMD mode decay rates ($\Lambda_{n,r}$) and oscillation frequencies ($\Lambda_{n,i}$) in Hz for the important low-order modes, $n = 1$, 2, 3, 5, 6, and 8.

Mode (n)	Decay rate ($\Lambda_{n,r}$) (Hz)	Oscillation frequency ($\Lambda_{n,i}$) (Hz)
1	−5.75	0
2	−57.64	0
3	−71.83	8.49
5	−72.47	0
6	−79.03	61.71
8	−80.32	40.48

Figure 14 shows the real component of the spatial distributions of coherent structures from the exact DMD modes, $\Theta^{\omega}_{r,n}$ for $n = 1$, 2, 3, 5, 6, and 8. The streamwise limits for the $\Theta^{\omega}_{r,n}$ fields were limited to $Y/D_h = 4$ since most coherent structure formations occur below this elevation. Mode 1, $\Theta^{\omega}_{r,1}$, shows similarities to the mean vorticity at VP1 for $Re = 6000$, as confirmed by Fig. 6(b). Smaller-scale instabilities were also observed at the peripheries of the $\Theta^{\omega}_{r,1}$ peaks, coincident with the interspatial ω peaks in Fig. 6(b) at VP1. This demonstrates non-oscillatory, steady flow with rotational structures localized within the shear layers of the jet structures, along with the turbulent instabilities in flow due to the spacer itself. Additionally, the non-oscillatory flow behavior described by the low-order spatial modes $\Theta^{\omega}_{r,2}$ and $\Theta^{\omega}_{r,5}$ also demonstrates the strong localization of spacer grid-induced turbulence below $Y/D_h = 2$.

This localization of turbulence for $0 < Y/D_h < 2$ is further observed in the dominant lower order modes $\Theta^{\omega}_{r,3}$, $\Theta^{\omega}_{r,6}$, and $\Theta^{\omega}_{r,8}$. These DMD modes confirm that the spacer grid induces minimal yet constricted turbulence in its immediate downstream vicinity, suggesting that the spacer grid functions primarily to affix the geometrical arrangement of the rod bundle and affirming that the transitional flow in the rod bundle leans toward laminar flow. The alternating maxima and minima due to the Kelvin–Helmholtz instabilities possess oscillation frequencies of 8.49, 61.71, and 40.48 Hz for the spatial modes $n = 3$, 6, and 8, respectively. The spatial modes along with their stability and oscillation characteristics demonstrate the capability of DMD in extracting spatial-temporally relevant flow structures—which although in this study yields confirmatory conclusions, demarcates the temporal characterization of dominant and concealed flow phenomena. Using the DMD analysis, the revealed underlying turbulence and momentum mechanisms are critical for the optimization of rod bundle and spacer grid geometries.

3. Flow reconstruction based on dynamic mode decomposition

An important application of DMD is reconstructing flow fields in a reduced-order basis using a significantly lower number of spatial modes and their respective eigenvalue-dependent temporal dynamics.[73] Flow reconstructions using reduced bases have significant computational benefits in terms of reduction of computational time, as highlighted in the studies by Han and Tan[80] and Li *et al.*[81] For the near-wall (VP1) instantaneous TR-PIV experimental spanwise (U_{inst}) and streamwise (V_{inst}) velocity fields, the DMD reconstruction was performed by first following the methodology listed in Sec. V B, and then evaluating the dynamic mode coefficients, b, as per

$$b_{k\times k} = \Theta^{\dagger}_{k\times k}\chi. \qquad (14)$$

Here, $\Theta^{\dagger}_{k\times k}$ is the Moore–Penrose pseudoinverse of the spatial modes, and χ is the TR-PIV velocity to be reconstructed (here, U_{rec} or V_{rec}). The approximate DMD reduced-order reconstruction at a given time instant, t, is obtained by evaluating

$$\chi(t) \approx b_{k\times k}\exp\left[t\cdot\log(\Lambda/\Delta t)\right]. \qquad (15)$$

The DMD reconstruction for any time instant may be performed by adjusting the truncation criteria, k. For the reconstructions demonstrated in this study, $k_1 = 50$ and $k_2 = 150$ were selected as the maximum truncated reduced order bases. This selection was considered to highlight the effects on reconstruction with different truncation criteria and to observe the resolution of the turbulent scales captured in the reconstructions. Figure 15 shows the comparison of the normalized instantaneous velocities at an arbitrary time instant with its normalized DMD reconstructed counterparts – for the spanwise velocity component, U/U_0 [Fig. 5(a)], and the streamwise component, V/U_0 [Fig. 5(b)]. The velocity magnitudes and directions are depicted by the vectors for all the flow fields in Fig. 15 for the 2 D region $-4.6 < X/D_h < 4.6$, $0 < Y/D_h < 6$.

The reconstructed velocity components in Fig. 15 represent accumulation of the dynamic mode coefficients up to k_1 and k_2 while incorporating the time dynamics as represented in Eq. (15). The reconstruction of U/U_0 [Fig. 15(a)] for k_1 captures only the most energy containing spanwise flow structures. The reduced-order spanwise velocity reconstructions for both k_1 and k_2 neglect the smaller turbulent scales, with a larger number of small-scale turbulent structures observed for k_2.[77] A higher number of small-scale turbulent structures were resolved for k_2 due to a larger number of modes capturing the energy contained in the smaller turbulent flow structures. Similarly, the reconstruction of the spanwise velocity fields (V/U_0) for k_1 and k_2 compared to the instantaneous V/U_0 in Fig. 15(b) indicate the capture of the full-field jet characteristics as they emanate from the spacer grid. Peripheral smoothing of the jet structures is a result of the reduced-order reconstructions capturing the most energy containing flow structures, once again neglecting the smaller turbulent scales which contain a lesser amount of the total flow energy.[78] The complex streamwise interactions are captured for both reconstructions with a larger amount of smaller interactions in the inter-jet regions seen for k_2, especially in the immediate downstream region of the spacer grid at $0 < Y/D_h < 1$. The presented DMD analysis complements the earlier analyses of time-averaged parameters and spatial–temporal correlations. DMD divulges important momentum and heat transport mechanisms critical for the design of LMFR rod bundle arrangements with spacer grids. The flow field reconstructions present reduced-order representations, which are critical in turbulence investigations to isolate the energy containing complex flow interactions based on several interlinked geometrical parameters, such as the spacer grid and the rod bundle. The capability of DMD to produce such reduced-order reconstructions benefits computational model development and validations when compared to experimental benchmarks, such as the analysis in this research.

VI. CONCLUSIONS

The presented experimental investigation in this study provides a comprehensive fluid dynamics investigation into the flow behavior within a 127-pin liquid metal fast reactor prototypical fuel assembly. 3D printed hexagonal honeycomb spacer grids were installed at axially defined intervals in the rod bundle to investigate nominal flow behavior. Time-resolved particle image velocimetry experiments were performed using the matched-index-of-refraction method to obtain non-intrusive velocity measurements at three axial planes in the downstream vicinity of the spacer grid at a Reynolds number condition of 6000. An uncertainty and convergence analysis was presented to verify the quality of the TR-PIV experimental data. For the instantaneous velocity fields, maximum normalized measurement uncertainties of 5.1% and 5.8% were obtained for the spanwise and streamwise components, respectively. Normalized first- and second-order velocimetry contours were presented to characterize and distinguish important flow features. The time-resolved velocity magnitude fields demonstrated the presence of jet flow structures emanating from the spacer grid, with a higher velocity at the near-wall plane. The interior subchannels in the rod bundle showed relative similarity in most velocimetry parameters, as previously assumed in the literature. Symmetry in the RMS spanwise and streamwise fluctuating velocity components

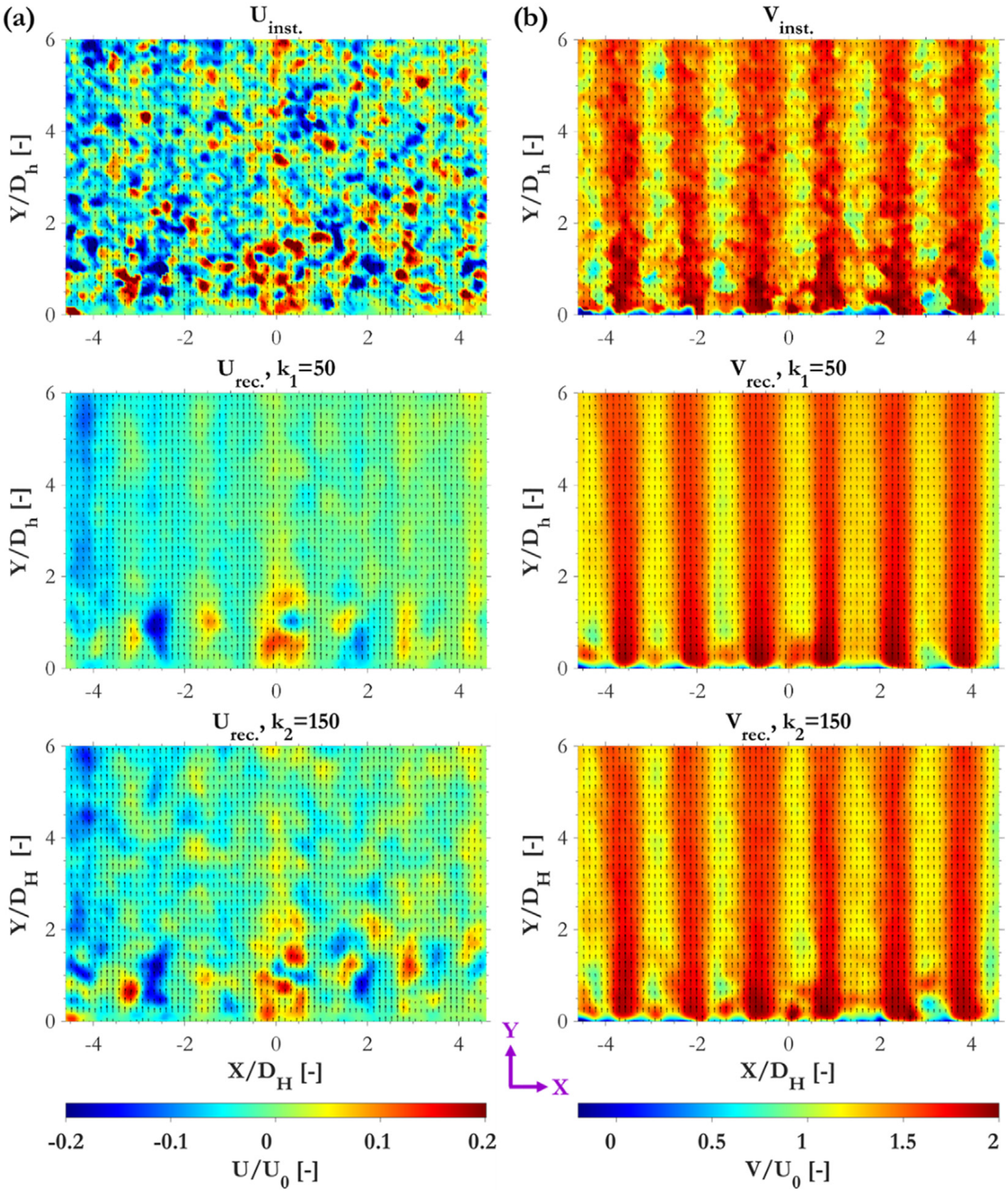

FIG. 15. Comparison between the instantaneous and DMD reconstructed velocity fields for the near-wall plane VP1 using truncated modes $k_1 = 50$ and $k_2 = 150$ for (a) normalized spanwise velocity (U/U_0), and (b) normalized streamwise velocity (V/U_0), both at arbitrary time instants.

was observed due to the regular geometry of the spacer grid and the rod bundle. Fluid shear layers at the jet structure peripheries were observed in the Reynolds shear stress 2D contours, which induced local fluid rotation as seen in the vorticity contours. Kelvin–Helmholtz fluid–fluid layer instabilities were observed in the interspatial region between the jet structure formations. The turbulence kinetic energy fields showed the localization of spacer grid-induced turbulence in the streamwise elevations of $0 < Y/D_h < 2$. To characterize the downstream flow progression, the line parameters were studied at three streamwise elevations of $Y/D_h = 0.5$, 2, and 10. Flow development was confirmed past an elevation of $Y/D_h = 4$ from the contour maps and the line profiles. The TR-PIV line profiles are an effective validation tool for computational models to describe fluid physics in an LMFR.

To study the spatial and temporal response of the velocity components, two-point spatial–temporal cross-correlations of the fluctuating velocity components were performed. Spatial cross-correlations without a time delay were utilized to analyze the spatial extent of local fluctuations. Alternating peaks were noticeable at spatial points known to lie along the boundary of fast and slow fluid flow streams, indicating shear layer effects and a small recirculation region due to the velocity gradient. Spatial–temporal cross-correlations with a time delay were computed in the axial direction at two locations, near the spacer grid and further downstream. The convection velocity of traveling vortices was approximated by the slope of the spatial–temporal correlation peaks. Near-wall flow in VP1 had a notably higher convection velocity due to bypass flow. Additionally, the fast and slow fluid streams had a noticeable effect in VP2 and VP3, whose points were located in the inter-jet flow transition spatial region.

Dynamic mode decomposition (DMD) analysis was applied to the TR-PIV instantaneous vorticity fields to extract mathematically dominant spatial–temporal descriptions of the flow in the near-wall PIV measurement window of the rod bundle. Important mode stability characteristics along with their temporal frequencies were quantified, along with representations of their respective spatial distributions. All the DMD modes for this study were observed to decay on temporal progression, and their respective rates of decay were quantified. The low-order spatial modes highlighted the important energy containing coherent structure formations and flow instabilities in the vicinity of the honeycomb spacer grid. The DMD analysis further confirmed the localization of turbulent instabilities within $0 < Y/D_h < 2$ for all the decomposed low-order spatial modes. The DMD analysis detailed spatiotemporally decomposed fluid dynamics portrait—by simultaneously quantifying their stability characteristics, decay rates, and oscillation frequencies. Truncating the modes to a reduced-order basis allowed a representation of the reconstructed spanwise and streamwise flow fields in the near-wall measurement plane, using the DMD reconstruction approach. Large-scale flow characteristics were demarcated in these reconstructed fields, which depended on the number of modes selected to reconstruct the velocity components, with smaller-scale turbulent structures excluded in the flow reconstructions due to their lower energy contributions. These experimental data sets present unique data sets which characterize the flow dynamics in past a honeycomb spacer grid in a 127-pin LMFR rod bundle prototype. The results provide high-fidelity experimental benchmarks for the validation of computational fluid dynamics models and reduced order models, imperative toward the development of LMFR spacer grid and rod bundle designs.

ACKNOWLEDGMENTS

This research was partially funded by U.S. Department of Energy—Nuclear Energy University Program (NEUP) Grant No. DE-FOA-0002128. The authors would like to acknowledge the efforts of Rodolfo Vaghetto, Se Ro Yang, Camila F. Matozinhos, and Alfred D. Carroll III toward experimental design and tests. The authors extend their gratitude to Paolo Ferroni, Milorad Dzodzo, and Elia Merzari for their productive technical discussions during this experimental campaign.

AUTHOR DECLARATIONS

Conflict of Interest

The authors have no conflicts to disclose.

Author Contributions

Craig Menezes: Formal analysis (lead); Investigation (lead); Methodology (lead); Software (lead); Visualization (lead); Writing – original draft (lead); Writing – review & editing (equal). **Trevor Melsheimer:** Formal analysis (supporting); Investigation (supporting); Software (supporting); Visualization (supporting); Writing – original draft (supporting); Writing – review & editing (equal). **Yassin Hassan:** Conceptualization (lead); Funding acquisition (lead); Methodology (equal); Project administration (lead); Resources (lead); Supervision (lead); Writing – review & editing (equal).

DATA AVAILABILITY

The data that support the findings of this study are available from the corresponding author upon reasonable request.

REFERENCES

[1] A. E. Waltar, D. R. Todd, and P. V. Tsvetkov, in *Fast Spectrum Reactors* (Springer, 2012), pp. 1–720.

[2] T. Sofu, "A review of inherent safety characteristics of metal alloy sodium-cooled fast reactor fuel against postulated accidents," Nucl. Eng. Technol. **47**(3), 227–239 (2015).

[3] H. Kim, H. Bae, Y. J. Ko, S. R. Choi, S. K. Chang, D. W. Lee, H. S. Choi, D. J. Euh, and H. Y. Lee, "Investigations of single-phase flow mixing characteristics in a wire-wrapped 37-pin bundle for a sodium-cooled fast reactor," Ann. Nucl. Energy **87**, 541–546 (2016).

[4] K. Rehme, "Pressure drop correlations for fuel element spacers," Nucl. Technol. **17**(1), 15–23 (1973).

[5] T. Nguyen and Y. Hassan, "Stereoscopic particle image velocimetry measurements of flow in a rod bundle with a spacer grid and mixing vanes at a low Reynolds number," Int. J. Heat Fluid Flow **67**, 202–219 (2017).

[6] P. Qi, X. Li, X. Li, S. Qiao, S. Tan, and Y. Chen, "Experimental study on the resistance characteristics of the rod bundle channel with spacer grid under low-frequency pulsating flows," Ann. Nucl. Energy **131**, 80–92 (2019).

[7] W. Qu, H. Xie, D. Shen, Z. Wang, and J. Xiong, "Experimental study of coherent structures downstream mixing vaned spacer grid of different inclination angles in a 5 × 5 rod bundle by TR-PIV," Ann. Nucl. Energy **181**, 109516 (2023).

[8] H. Yuan, M. A. Yildiz, E. Merzari, Y. Yu, A. Obabko, G. Botha, G. Busco, Y. A. Hassan, and D. T. Nguyen, "Spectral element applications in complex nuclear reactor geometries: Tet-to-hex meshing," Nucl. Eng. Des. **357**, 110422 (2020).

[9] T. Nguyen, N. Goth, P. Jones, R. Vaghetto, and Y. Hassan, "Stereoscopic PIV measurements of near-wall flow in a tightly packed rod bundle with wire spacers," Exp. Therm. Fluid Sci. **92**, 420–435 (2018).

[10] T. Nguyen, N. Goth, P. Jones, S. Lee, R. Vaghetto, and Y. Hassan, "PIV measurements of turbulent flows in a 61-pin wire-wrapped hexagonal fuel bundle," Int. J. Heat Fluid Flow **65**, 47–59 (2017).

[11] T. Nguyen, R. Vaghetto, and Y. Hassan, "Experimental investigation of turbulent wake flows in a helically wrapped rod bundle in presence of localized blockages," Phys. Fluids **32**(7), 075113 (2020).

[12] M. Childs, R. Vaghetto, P. Jones, N. Goth, and Y. Hassan, "Experimental determination and analysis of the transverse pressure difference in a wire-wrapped rod bundle," Int. J. Heat Mass Transfer **170**, 120958 (2021).

[13] M. Childs, R. Muyshondt, R. Vaghetto, D. T. Nguyen, and Y. Hassan, "Experimental study on the effect of localized blockages on the friction factor of a 61-pin wire-wrapped bundle," J. Fluids Eng., Trans. ASME **142**(11), 111211 (2020).

[14] C. Menezes, R. Vaghetto, and Y. A. Hassan, "Experimental investigation of the subchannel axial pressure drop and hydraulic characteristics of a 61-pin wire wrapped rod bundle," J. Fluids Eng., Trans. ASME **144**(5), 1–9 (2022).

[15] C. Menezes, T. Melsheimer, D. W. Pyle, M. Kinsky, and Y. A. Hassan, "Flow characteristics within an interior subchannel of a 61-pin wire-wrapped hexagonal rod bundle with a porous blockage," Phys. Fluids **35**(2), 027106 (2023).

[16] J. Pacio, M. Daubner, F. Fellmoser, K. Litfin, and T. Wetzel, "Experimental study of heavy-liquid metal (LBE) flow and heat transfer along a hexagonal 19-rod bundle with wire spacers," Nucl. Eng. Des. **301**, 111–127 (2016).

[17] J. Pacio, M. Daubner, F. Fellmoser, K. Litfin, and T. Wetzel, "Heat transfer experiment in a partially (internally) blocked 19-rod bundle with wire spacers cooled by LBE," Nucl. Eng. Des. **330**, 225–240 (2018).

[18] M. Song, J. H. Jeong, and E. S. Kim, "Investigation on subchannel flow distribution in wire-wrapped 37 and 61-pin bundle using computational fluid dynamics," Nucl. Eng. Des. **370**, 110904 (2020).

[19] M. S. Song, J. H. Jeong, and E. S. Kim, "Numerical investigation on vortex behavior in wire-wrapped fuel assembly for a sodium fast reactor," Nucl. Eng. Technol. **51**(3), 665–675 (2019).

[20] M. S. Song, J. H. Jeong, and E. S. Kim, "Flow visualization on SFR wire-wrapped 19-pin bundle geometry using MIR-PIV-PLIF and comparisons with RANS-based CFD analysis," Ann. Nucl. Energy **147**, 107653 (2020).

[21] R. Vaghetto, P. Jones, N. Goth, M. Childs, S. Lee, D. Thien Nguyen, and Y. A. Hassan, "Pressure measurements in a wire-wrapped 61-pin hexagonal fuel bundle," J. Fluids Eng. **140**(3), 1–9 (2018).

[22] F. Bertocchi, M. Rohde, and J. L. Kloosterman, "Experimental investigation on the influence of gap vortex streets on fluid-structure interactions in hexagonal bundle geometries," Int. J. Heat Fluid Flow **79**, 108443 (2019).

[23] R. Gajapathy, K. Velusamy, P. Selvaraj, P. Chellapandi, and S. C. Chetal, "A comparative CFD investigation of helical wire-wrapped 7, 19 and 37 fuel pin bundles and its extendibility to 217 pin bundle," Nucl. Eng. Des. **239**(11), 2279–2292 (2009).

[24] A. Batta and A. G. Class, "CFD analysis of pressure drop across grid spacers in rod bundles compared to correlations and heavy liquid metal experimental data," Nucl. Eng. Des. **312**, 121–127 (2017).

[25] A. Mathur, H. Uitslag-Doolaard, and F. Roelofs, "Reduced-resolution RANS approach to grid spacer fuel assemblies," Nucl. Eng. Des. **356**, 110374 (2020).

[26] K. Sergeenko, K. Svirid, D. Afremov, and V. Folomeev, "Demonstration of the model of physicochemical processes in heavy liquid metal cooled reactors in an example of the THEADES experiment simulation," Nucl. Eng. Des. **395**, 111870 (2022).

[27] J. Pacio, M. Daubner, F. Fellmoser, K. Litfin, L. Marocco, R. Stieglitz, S. Taufall, and T. Wetzel, "Heavy-liquid metal heat transfer experiment in a 19-rod bundle with grid spacers," Nucl. Eng. Des. **273**, 33–46 (2014).

[28] J. Pacio, K. Litfin, A. Batta, M. Viellieber, A. Class, H. Doolaard, F. Roelofs, S. Manservisi, F. Menghini, and M. Böttcher, "Heat transfer to liquid metals in a hexagonal rod bundle with grid spacers: Experimental and simulation results," Nucl. Eng. Des. **290**, 27–39 (2015).

[29] R. Marinari, I. Di Piazza, M. Tarantino, and N. Forgione, "Blockage fuel pin simulator experiments and simulation," Nucl. Eng. Des. **353**, 110215 (2019).

[30] D. Martelli, N. Forgione, I. Di Piazza, and M. Tarantino, "HLM fuel pin bundle experiments in the CIRCE pool facility," Nucl. Eng. Des. **292**, 76–86 (2015).

[31] K. Rehme and G. Trippe, "Pressure drop and velocity distribution in rod bundles with spacer grids," Nucl. Eng. Des. **62**(1–3), 349–359 (1980).

[32] C. Menezes, A. D. Carroll, C. F. Matozinhos, R. Vaghetto, and Y. A. Hassan, "Turbulent flow characteristics in an 84-pin rod bundle for typical and damaged spacer grids," Phys. Fluids **34**(5), 055103 (2022).

[33] C. F. Matozinhos, A. D. Carroll, C. Menezes, R. Vaghetto, and Y. Hassan, "Experimental measurements of fluid flow in an 84-pin hexagonal rod bundle with spacer grid for a gas-cooled fast modular reactor," Int. J. Heat Fluid Flow **97**, 109014 (2022).

[34] T. Nguyen, R. Muyshondt, Y. A. Hassan, and N. K. Anand, "Experimental investigation of cross flow mixing in a randomly packed bed and streamwise vortex characteristics using particle image velocimetry and proper orthogonal decomposition analysis," Phys. Fluids **31**(2), 025101 (2019).

[35] W. Qu, J. Xiong, S. Chen, and X. Cheng, "High-fidelity PIV measurement of cross flow in 5 × 5 rod bundle with mixing vane grids," Nucl. Eng. Des. **344**, 131–143 (2019).

[36] N. Amini and Y. A. Hassan, "Measurements of jet flows impinging into a channel containing a rod bundle using dynamic PIV," Int. J. Heat Mass Transfer **52**(23–24), 5479–5495 (2009).

[37] N. Goth, P. Jones, T. Duy Nguyen, R. Vaghetto, Y. Hassan, N. Salpeter, and E. Merzari, "PTV/PIV measurements of turbulent flows in interior subchannels of a 61-pin wire-wrapped hexagonal fuel bundle," Int. J. Heat Fluid Flow **71**, 295–304 (2018).

[38] H. M. McIlroy, D. M. McEligot, and R. J. Pink, "Measurement of turbulent flow phenomena for the lower plenum of a prismatic gas-cooled reactor," Nucl. Eng. Des. **240**(2), 416–428 (2010).

[39] D. Orea, R. Vaghetto, T. Nguyen, and Y. Hassan, "Experimental measurements of flow mixing in cold leg of a pressurized water reactor," Ann. Nucl. Energy **140**, 107137 (2020).

[40] A. A. Campagnole dos Santos, M. Childs, T. D. Nguyen, and Y. Hassan, "Convergence study and uncertainty quantification of average and statistical PIV measurements in a matched refractive index 5 × 5 rod bundle with mixing vane spacer grid," Exp. Therm. Fluid Sci. **102**, 215–231 (2019).

[41] M. Samimy and A. L. Addy, "Interaction between two compressible, turbulent free shear layers," AIAA J. **24**(12), 1918–1923 (1986).

[42] M. Raffel, C. E. Willert, F. Scarano, C. J. Kähler, S. T. Wereley, and J. Kompenhans, *Particle Image Velocimetry: A Practical Guide* (Springer, 2018).

[43] J. Pacio, S. K. Chen, Y. M. Chen, and N. E. Todreas, "Analysis of pressure losses and flow distribution in wire-wrapped hexagonal rod bundles for licensing. Part I: The Pacio-Chen-Todreas Detailed model (PCTD)," Nucl. Eng. Des. **388**, 111607 (2022).

[44] J. Pacio, S. K. Chen, Y. M. Chen, and N. E. Todreas, "Analysis of pressure losses and flow distribution in wire-wrapped hexagonal rod bundles for licensing. Part II: Evaluation of public experimental data," Nucl. Eng. Des. **388**, 111606 (2022).

[45] A. Eckstein and P. P. Vlachos, "Assessment of advanced windowing techniques for digital particle image velocimetry (DPIV)," Meas. Sci. Technol. **20**(7), 075402 (2009).

[46] A. Eckstein and P. P. Vlachos, "Digital particle image velocimetry (DPIV) robust phase correlation," Meas. Sci. Technol. **20**(5), 055401 (2009).

[47] J. Westerweel, "Efficient detection of spurious vectors in particle image velocimetry data," Exp. Fluids **16–16**, 236–247 (1994).

[48] T. Nguyen, L. White, R. Vaghetto, and Y. Hassan, "Turbulent flow and vortex characteristics in a blocked subchannel of a helically wrapped rod bundle," Exp. Fluids **60**(8), 1–28 (2019).

[49] J. J. Charonko and P. P. Vlachos, "Estimation of uncertainty bounds for individual particle image velocimetry measurements from cross-correlation peak ratio," Meas. Sci. Technol. **24**(6), 065301 (2013).

[50] B. M. Wilson and B. L. Smith, "Uncertainty on PIV mean and fluctuating velocity due to bias and random errors," Meas. Sci. Technol. **24**(3), 035302 (2013).

[51] D. R. Neal, A. Sciacchitano, B. L. Smith, and F. Scarano, "Collaborative framework for PIV uncertainty quantification: The experimental database," Meas. Sci. Technol. **26**(7), 074003 (2015).

[52] A. Sciacchitano and B. Wieneke, "PIV uncertainty propagation," Meas. Sci. Technol. **27**(8), 084006 (2016).

[53] A. Sciacchitano, D. R. Neal, B. L. Smith, S. O. Warner, P. P. Vlachos, B. Wieneke, and F. Scarano, "Collaborative framework for PIV uncertainty quantification: Comparative assessment of methods," Meas. Sci. Technol. **26**(7), 074004 (2015).

[54] R. Muyshondt, T. Nguyen, Y. A. Hassan, and N. K. Anand, "Experimental measurements of the wake of a sphere at subcritical Reynolds numbers," J. Fluids Eng. **143**(6), 1–19 (2021).

[55] R. Muyshondt, N. K. Anand, Y. A. Hassan, and T. Nguyen, "Flow and heat transfer in the wake of a triangular arrangement of spheres," Phys. Fluids **33**(11), 115127 (2021).

[56] A. Assoudi, N. Mahjoub Saïd, H. Bournot, and G. Le Palec, "Comparative study of flow characteristics of a single offset jet and a turbulent dual jet," Heat Mass Transfer **55**(4), 1109–1131 (2019).

[57] S. K. Chen, Y. M. Chen, and N. E. Todreas, "The upgraded Cheng and Todreas correlation for pressure drop in hexagonal wire-wrapped rod bundles," Nucl. Eng. Des. **335**, 356–373 (2018).

[58] P. J. Kristo and M. L. Kimber, "Cylinders and jets in crossflow: Wake formations as a result of varying geometric proximities," Phys. Fluids **33**(5), 055106 (2021).

[59] F. Kerhervé and J. Fitzpatrick, "Measurement and analysis of the turbulent length scales in jet flows," Exp. Fluids **50**(3), 637–651 (2011).

[60] J. L. Lumley, "Coherent structures in turbulence," *Transition and Turbulence* (Academic Press, 1981), pp. 215–242.

[61] K. Taira, S. L. Brunton, S. T. M. Dawson, C. W. Rowley, T. Colonius, B. J. McKeon, O. T. Schmidt, S. Gordeyev, V. Theofilis, and L. S. Ukeiley, "Modal analysis of fluid flows: An overview," AIAA J. **55**(12), 4013–4041 (2017).

[62] G. Berkooz, P. Holmes, and J. L. Lumley, "The proper orthogonal, decomposition in the analysis of turbulent flows," Annu. Rev. Fluid Mech. **25**(1971), 539–575 (1993).

[63] S. Ullmann, M. Rotkvic, and J. Lang, "POD-Galerkin reduced-order modeling with adaptive finite element snapshots," J. Comput. Phys. **325**, 244–258 (2016).

[64] M. Liu, L. Tan, and S. Cao, "Dynamic mode decomposition of cavitating flow around ALE 15 hydrofoil," Renewable Energy **139**, 214–227 (2019).

[65] P. J. Schmid, "Application of the dynamic mode decomposition to experimental data," Exp. Fluids **50**(4), 1123–1130 (2011).

[66] P. J. Schmid, "Dynamic mode decomposition of numerical and experimental data," J. Fluid Mech. **656**, 5–28 (2010).

[67] T. Nguyen, E. Kappes, S. King, Y. Hassan, and V. Ugaz, "Time-resolved PIV measurements in a low-aspect ratio facility of randomly packed spheres and flow analysis using modal decomposition," Exp. Fluids **59**(8), 1–29 (2018).

[68] J. N. Kutz, X. Fu, and S. L. Brunton, "Multiresolution dynamic mode decomposition," SIAM J. Appl. Dyn. Syst. **15**(2), 713–735 (2016).

[69] N. Benjamin Erichson, L. Mathelin, J. N. Kutz, and S. L. Brunton, "Randomized dynamic mode decomposition," SIAM J. Appl. Dyn. Syst. **18**(4), 1867–1891 (2019).

[70] M. R. Jovanović, R. Mihailo, P. J. Schmid, and J. W. Nichols, "Sparsity-promoting dynamic mode decomposition," Phys. Fluids **26**(2), 024103 (2021).

[71] K. K. Chen, J. H. Tu, and C. W. Rowley, "Variants of dynamic mode decomposition: Connections between Koopman and Fourier analyses," J. Nonlinear Sci. **22**, 887–915 (2012).

[72] J. Garicano-Mena, B. Li, E. Ferrer, and E. Valero, "A composite dynamic mode decomposition analysis of turbulent channel flows," Phys. Fluids **31**(11), 115102 (2019).

[73] J. N. Kutz, S. L. Brunton, B. W. Brunton, and J. L. Proctor, *Dynamic mode decomposition: data-driven modeling of complex systems* (Society for Industrial and Applied Mathematics, 2016).

[74] J. H. Tu, C. W. Rowley, D. M. Luchtenburg, S. L. Brunton, and J. N. Kutz, "On dynamic mode decomposition: Theory and applications," J. Comput. Dyn. **1**(2), 391–421 (2014).

[75] D. A. Bistrian and I. M. Navon, "An improved algorithm for the shallow water equations model reduction: Dynamic Mode Decomposition vs POD," Int. J. Numer. Methods Fluids **78**, 552–580 (2015).

[76] C. Y. Li, Z. Chen, T. K. T. Tse, A. U. Weerasuriya, X. Zhang, Y. Fu, and X. Lin, "A parametric and feasibility study for data sampling of the dynamic mode decomposition: Spectral insights and further explorations," Phys. Fluids **34**(3), 035102 (2022).

[77] Y. Liu, Q. Wu, B. Huang, H. Zhang, W. Liang, and G. Wang, "Decomposition of unsteady sheet/cloud cavitation dynamics in fluid-structure interaction via POD and DMD methods," Int. J. Multiphase Flow **142**, 103690 (2021).

[78] M. Zhao, Y. Zhao, and Z. Liu, "Dynamic mode decomposition analysis of flow characteristics of an airfoil with leading edge protuberances," Aerosp. Sci. Technol. **98**, 105684 (2020).

[79] J. H. Tu, "Dynamic Mode Decomposition: Theory and Applications," Ph.D. dissertation (Princeton University, 2013).

[80] Y. Han and L. Tan, "Dynamic mode decomposition and reconstruction of tip leakage vortex in a mixed flow pump as turbine at pump mode," Renewable Energy **155**, 725–734 (2020).

[81] C. Y. Li, T. K. T. Tse, and G. Hu, "Dynamic mode decomposition on pressure flow field analysis: flow field reconstruction, accuracy, and practical significance," J. Wind Eng. Ind. Aerodyn. **205**, 104278 (2020).